

Electronic Thesis and Dissertation Repository

10-20-2016 12:00 AM

Neurosurgical Ultrasound Pose Estimation Using Image-Based Registration and Sensor Fusion - A Feasibility Study

Utsav Pardasani

The University of Western Ontario

Supervisor

Dr. Terry Peters

The University of Western Ontario Joint Supervisor

Dr. Ali Khan

The University of Western Ontario

Graduate Program in Biomedical Engineering

A thesis submitted in partial fulfillment of the requirements for the degree in Master of Engineering Science

© Utsav Pardasani 2016

Follow this and additional works at: <https://ir.lib.uwo.ca/etd>



Part of the [Artificial Intelligence and Robotics Commons](#), [Biomedical Devices and Instrumentation Commons](#), [Surgical Procedures, Operative Commons](#), and the [Systems and Integrative Engineering Commons](#)

Recommended Citation

Pardasani, Utsav, "Neurosurgical Ultrasound Pose Estimation Using Image-Based Registration and Sensor Fusion - A Feasibility Study" (2016). *Electronic Thesis and Dissertation Repository*. 4194.

<https://ir.lib.uwo.ca/etd/4194>

This Dissertation/Thesis is brought to you for free and open access by Scholarship@Western. It has been accepted for inclusion in Electronic Thesis and Dissertation Repository by an authorized administrator of Scholarship@Western. For more information, please contact wlsadmin@uwo.ca.

Abstract

Modern neurosurgical procedures often rely on computer-assisted real-time guidance using multiple medical imaging modalities. State-of-the-art commercial products enable the fusion of pre-operative with intra-operative images (e.g., magnetic resonance [MR] with ultrasound [US] images), as well as the on-screen visualization of procedures in progress¹⁻⁴. In so doing, US images can be employed as a template to which pre-operative images can be registered, to correct for anatomical changes, to provide live-image feedback, and consequently to improve confidence when making resection margin decisions near eloquent regions during tumour surgery^{1,5,6}.

In spite of the potential for tracked ultrasound to improve many neurosurgical procedures, it is not widely used. State-of-the-art systems are handicapped by optical tracking's need for consistent line-of-sight, keeping tracked rigid bodies clean and rigidly fixed, and requiring a calibration workflow. The goal of this work is to improve the value offered by co-registered ultrasound images without the workflow drawbacks of conventional systems. The novel work in this thesis includes:

- the exploration and development of a GPU-enabled 2D-3D multi-modal registration algorithm based on the existing LC2 metric; and
- the use of this registration algorithm in the context of a sensor and image-fusion algorithm.

The work presented here is a motivating step in a vision towards a heterogeneous tracking framework for image-guided interventions where the knowledge from intraoperative imaging, pre-operative imaging, and (potentially disjoint) wireless sensors in the surgical field are seamlessly integrated for the benefit of the surgeon. The technology described in this thesis, inspired by advances in robot localization demonstrate how inaccurate pose data from disjoint sources can produce a localization system greater than the sum of its parts.

Keywords: Multi-Modal Medical Image Registration, Image Guided Neurosurgery, Magnetic Resonance Imaging, Ultrasound, Medical Imaging, Robot Localization

Co-Authorship Statement

Portions of the introduction to this thesis were present in a project for the Image Guided Intervention's class and were submitted to Dr. Terry Peters for course credit under the title "Applications of Mixed Reality to Neurosurgical Procedures," with portions written by Adam Rankin and Szymon Kowal.

The work in Chapter 2 is adapted from the paper U **Pardasani**, JSH Baxter, TM Peters and AR Khan, *Single slice US-MRI registration for neurosurgical MRI-guided US* SPIE Medical Imaging, 2016. I conceived, implemented, and executed the work described in the paper. John Baxter and I developed the BOXLC2 similarity metric on a coffee break. John Baxter also provided essential advice aiding with the CUDA implementations of the similarity metrics that were tested. Both Ali Khan and John Baxter aided with directing my experiment efforts. All co-authors aided with the review of this thesis and provided valuable discussions.

The work in Chapter 3 was conceived, implemented, and executed by me. I benefitted from help with data collection for the phantom experiments from Ali Khan, Adam Rankin, Loxlan Kasa, Jonathan Lau, Golafsoun Ameri, and John Baxter. The work described in Chapter 3 partially appears in a patent that has been filed and co-authored with Ali Khan.

All the work in this thesis benefitted from valuable discussions in the VASST lab, and Synaptive Medical. Finally, this thesis has benefitted from the editing efforts of my wife, Annick MacAskill.

Acknowledgements

My story in Dr. Terry Peters' lab began over 12 years ago, when I was in high school. I had just completed a co-op term in Dr. Jim Johnson's lab under Dr. Louis Ferriera's supervision, when my friend Dr. Pencilla Lang recommended that I get in touch with Dr. Peters for summer work. At that point I had just finished some code to visualize the motion of cadaveric arms in VTK and Python, and was keen to do more with those essential APIs that were partly being developed in Terry's lab. I of course came back for my first university co-op term too! At that time, I had no idea how seminal the work being done in Dr. Peters' lab was. In this thesis I am proud to cite the work that was happening around me at that time, though I lacked the bearings to understand it then. Not only did Dr. Peters give me that amazing exposure early on, but he also provided me with a glowing recommendation when I was job hunting after my undergraduate studies (though it meant delaying graduate studies under his guidance).

I am also thankful for Dr. Ali Khan. When things got stuck, and I got stuck, Ali got creative. At the start of my degree, Ali brought enthusiasm to my foray into neuroimaging and neurosurgical interventions. Ali very patiently gave me reassurance, comfort, and guidance every time my code was misbehaving. Ali seems to know enough about everything to make things better, and I am proud to call Ali my supervisor.

I am thankful for the entirety of the VASST lab. Each one of you brought something important to my degree. I am shy to mention names at risk of neglecting one of you. Sometimes at night I worry that I have taken more from you all than I have given. I am in your debt.

I would also like to thank Gal Sela and my colleagues at Synaptive Medical. Your mentorship and comradery throughout my thesis has meant much to enrich this learning experience. At the time when I was focussing on the details of the work described here, they were there to remind me of the big picture of neurosurgical interventions.

My parents get a big thanks for their support throughout my life. Anything I have done well is a credit to the many insights (technical and non-technical) they have shared with me. I would also like to thank my sister, Dr. Avni Pardasani, for her unfailing encouragement.

Finally, I'd like to thank my wife Annick, who helped keep my head on this planet (Earth, that is) when it was lost in the search space of my thesis and the work described here. She is my ultimate support in more ways than I can list.

Table of Contents

| | |
|---|------|
| Abstract..... | i |
| Co-Authorship Statement..... | ii |
| Acknowledgements..... | iii |
| Table of Contents..... | v |
| List of Tables..... | viii |
| List of Figures..... | ix |
| Chapter 1..... | 1 |
| 1 Image-Guided Neurosurgery..... | 1 |
| 1.1 Biopsy..... | 2 |
| 1.2 Tumour Resection..... | 3 |
| 1.3 Common Challenges..... | 4 |
| 1.3.1 Registration Error and Brain Shift..... | 4 |
| 1.3.2 Human Factors..... | 5 |
| 1.3.3 Sterile Field / Reprocessing..... | 5 |
| 1.4 Stereotactic Frame..... | 6 |
| 1.5 Frameless Stereotaxy..... | 7 |
| 1.5.1 Optical Tracking Error in Frameless Stereotaxy..... | 8 |
| 1.6 Intraoperative Imaging..... | 10 |
| 1.7 Ultrasound in Neurosurgery..... | 10 |
| 1.7.1 Ultrasound Imaging Considerations..... | 14 |
| 1.8 System Design..... | 15 |
| 1.9 Image-Based Registration..... | 17 |
| 1.9.1 Multimodal US/MRI Image Based Registration in Neurosurgery..... | 19 |
| 1.10 Other Pose Estimation methods..... | 20 |

| | | |
|-----------|--|----|
| 1.10.1 | Sensor/Data fusion with Kalman Filtering | 21 |
| 1.11 | Summary | 24 |
| Chapter 2 | | 25 |
| 2 | 2D/3D US – MRI Slice to Volume Registration..... | 25 |
| 2.1 | Background..... | 25 |
| 2.2 | Methods..... | 26 |
| 2.2.1 | Overview..... | 26 |
| 2.2.2 | GPU LC2 Implementation | 26 |
| 2.2.3 | Boxcar Filter Normalized LC2 (BOXLC2) | 27 |
| 2.2.4 | Particle Swarm Optimizer..... | 29 |
| 2.3 | Testing Approach..... | 30 |
| 2.4 | Results..... | 33 |
| 2.4.1 | 3DOF Pose Recovery..... | 33 |
| 2.4.2 | 6DOF Pose Recovery via Particle Swarm Optimization | 34 |
| 2.5 | Discussion..... | 37 |
| Chapter 3 | | 39 |
| 3 | An Unscented Kalman Filter Multi-Data Fusion Algorithm for Neurosurgical Ultrasound Guidance..... | 39 |
| 3.1 | Background..... | 39 |
| 3.2 | Methods..... | 40 |
| 3.2.1 | Overview..... | 40 |
| 3.2.2 | Unscented Kalman Filtering and Smoothing..... | 40 |
| 3.2.3 | Particle Swarm Optimizer..... | 41 |
| 3.2.4 | Simulated Data..... | 41 |
| 3.2.5 | Phantom Experiments | 42 |
| 3.2.6 | Analysis..... | 43 |

| | |
|--|----|
| 3.2.7 MRI-Guided Neurosurgical Ultrasound with Image-Registration and Inertial Tracking Only..... | 43 |
| 3.2.8 Line of Sight Correction in an MRI-Guided Ultrasound System Using Inertial Measurements and Image-Based Registration | 44 |
| 3.2.9 Analysis..... | 44 |
| 3.3 Results..... | 44 |
| 3.3.1 Line of Sight Correction Using UKF Algorithm | 44 |
| 3.3.2 MRI-Guided Ultrasound Without a Conventional Tracking System | 48 |
| 3.3.3 Phantom Experiment Results..... | 52 |
| 3.4 Discussion..... | 57 |
| Chapter 4..... | 59 |
| 4 Conclusions | 59 |
| 4.1 Future Work | 60 |
| Bibliography | 62 |
| Curriculum Vitae | 73 |

List of Tables

| | |
|---|----|
| Table 1: Summary of image modalities available for intraoperative guidance | 9 |
| Table 2: Neurosurgical ultrasound semieology per Prada et al. | 15 |
| Table 3: Slice-target pairs used in my experiments | 31 |
| Table 4. Results from image-based registration, solving for translation components with orientation used from original dataset..... | 35 |
| Table 5: Mean TRE values associated with slice-based registration solving for the full pose of the US probe | 37 |
| Table 6: Comparing TRE histograms between the UKF sensor fusion line-of-sight correction algorithms to the original data. | 45 |
| Table 7: Comparing TRE histograms between the UKF sensor fusion pose estimation algorithms to the original data. | 49 |

List of Figures

| | |
|--|----|
| Figure 1: Technologies that inform an image-guided neurosurgery’s activities | 1 |
| Figure 2: Tracked ultrasound-guided biopsy | 3 |
| Figure 3: Conventional tracked ultrasound operating room layout | 12 |
| Figure 4: Registration similarity metric function..... | 18 |
| Figure 5: Hidden Markov Model representation of the evolution of states (x(t)) and their measurements (y(t)) in a pose measurement and estimation problem..... | 22 |
| Figure 6: Kalman filter algorithm steps | 23 |
| Figure 7: Example Kalman filtering pseudocode | 23 |
| Figure 8: Pseudocode for LC2 GPU kernel | 27 |
| Figure 9: The voxelwise evaluation of $f(\Psi, x_i)$ creates simulated ultrasound image that resemble boxcar filtered US image as image dissimilarity increases | 28 |
| Figure 10: Pseudocode for BOXLC2 GPU kernel..... | 28 |
| Figure 11: Particle swarm iteration pseudo-code..... | 29 |
| Figure 12: Histogram of TRE values associated with slice-target pairs in the subset of the targets from the BITE dataset (errors >5mm are not shown) | 31 |
| Figure 13: Comparison of BOXLC2 and LC2 with varying patch sizes and downsampling ratios resulting in different TREs and kernel execution speeds..... | 33 |
| Figure 14: Histogram of TRE values for slice-target pairs in the BITE dataset from conducting a craniotomy-site constrained registration in 3DOF..... | 35 |
| Figure 15: Some example cases from the slice based registration algorithm with calculated pose results (brown) and original pose results (purple) shown in 3D (left column) alongside the original ultrasound image (centre-left column), reformatted MRI slice corresponding to the | |

| | |
|---|----|
| calculated US pose (centre-right column), and reformatted MRI slice corresponding to the original US pose (right column) | 36 |
| Figure 16: Histogram of TRE values for slice-target pairs with poses resulting from Particle Swarm optimization with the BOXLC2 metric (slice-target pairs with TRE values >5mm are not shown)..... | 37 |
| Figure 17: Multi-Modal Phantom (left) and ultrasound probe instrumented with IMU and optical tracker (Right)..... | 43 |
| Figure 18: MR slice from original optical tracking pose (top left) alongside original ultrasound image (top right), patchwise similarity metric weight (bottom centre), and patchwise unweighted similarity (bottom left) | 54 |
| Figure 19: MR slice matching original US pose from BITE dataset (top left) alongside ultrasound image (top right), patchwise similarity metric weight (bottom centre), and patchwise unweighted similarity (bottom left) | 55 |
| Figure 20: Histogram of distances from UKF algorithm pose to optical tracking pose | 55 |
| Figure 21: BOXLC2 similarity metric search space visualizations centered around the optical tracking pose in two of the failure cases showing unclear optimas in the similarity function in the translation components | 56 |
| Figure 22: Spatial distortion in MRI image volume | 56 |
| Figure 23: Example ultrasound image registered to MRI volume using optical tracking with manually placed landmarks in common co-ordinate space for visualization | 57 |
| Figure 24: A multi-sensor fusion tracked biopsy forcep using image-based tracking, inertial measurements, and an ultrasonic range finder | 61 |

Chapter 1

1 Image-Guided Neurosurgery

Neurosurgery spans many procedures that include both the brain and spine. For the purpose of this thesis, the focus will be on cerebral procedures. The majority of cerebral neurosurgical procedures are image-guided, i.e., they include some kind of medical imaging done before, during, and/or after the surgery to inform and evaluate the procedure.

A typical image-guided neurosurgical procedure can be divided into the following activities:

| Modality/ Technology | | Surgery Phase |
|----------------------|---------------------------------------|--|
| Pre-Op Imaging | Surgical Navigation with Pre-Op Image | 1) <i>Planning</i> Identify a region for treatment. Plan a path for an interventional tool. Some key parameters may be determined intra-operatively. |
| | | 2) <i>Navigating</i> Guide the tool/treatment device to the region of interest. Verify the location if possible. |
| | | 3) <i>Treatment and monitoring</i> Apply and monitor the treatment. |
| | Intra-Op Imaging | 4) <i>Verifying</i> Verify that the treatment adhered to the planned procedure and had the intended effect. |
| | Post-Op Imaging | |

Figure 1: Technologies that inform an image-guided neurosurgery’s activities

Per Figure 1, the role of surgical tracking and intraoperative imaging is seen to be invaluable for the procedure. Intraoperative imaging can update the surgeon's knowledge of a surgical site in real-time, providing critical feedback regarding the navigation and localization of surgical tools, especially in the context of the inevitable anatomic changes that occur in neurosurgery. Consequently, there has been much promising work investigating the application of ultrasound as an effective intraoperative imaging modality for neurosurgery, with some work even showing gains comparable to using intra-operative MRI⁵. Even then, ultrasound imaging is not the norm in neurosurgical operating rooms, in part due to major workflow handicaps and the difficulty that arises in its interpretation. It is the goal of my work to develop enabling technologies to ameliorate some of these technical and workflow issues.

The breadth and variety of neurosurgical procedures is large. In this thesis, I have chosen to narrow the discussion to intracranial tumour resection and tumour biopsy, though the technologies developed have applicability to other procedures.

1.1 Biopsy

If a region of interest (ROI) identified in the pre-operative image is suspected to be a malignant brain tumour, it is often desirable to perform a biopsy in order to develop a diagnosis from a histological sample. In this situation, the guidance of the biopsy needle to an ROI can be challenging, as the size and depth of the ROI can affect the ability of the surgeon to find it⁷. In addition, there is a risk of hemorrhaging, the consequences of which grow more serious as the target approaches the brainstem⁸.

Complication rates for biopsies vary widely in the literature, which suggests that there is a strong element of skill with regards to candidate selection, trajectory planning, and guidance^{9,10}.

The incorporation of functional information in these procedures allows surgeons to avoid critical brain areas. The fusion of needle position with pre-operative images from multiple modalities is a challenging task. In this situation, the needle may be physically

moving in a direction that is spatially incompatible with what is being shown on the display, causing undue mental strain for the surgeon.

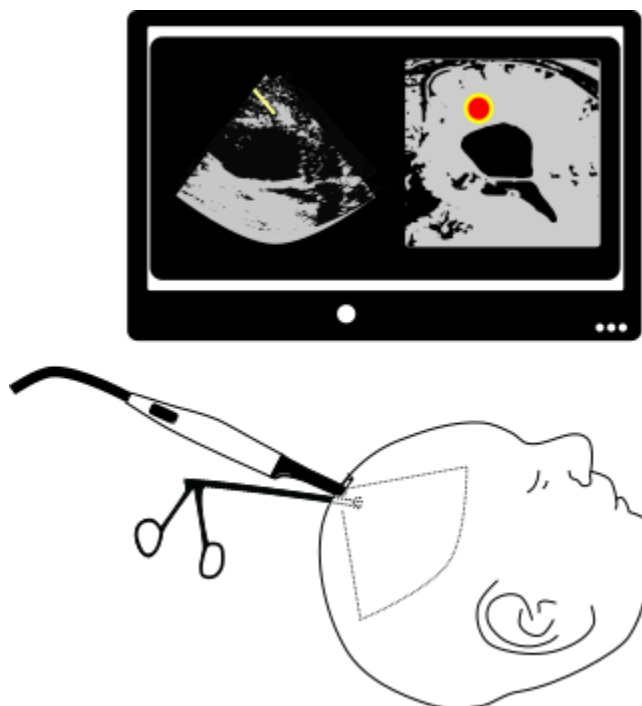


Figure 2: Tracked ultrasound-guided biopsy

Intraoperative imaging with ultrasound can give real-time feedback for the localization of the biopsy forceps^{4,11}. Doppler imaging can help identify vessels, and real-time oblique transformation of the MRI volume to show the matching US slice can help decipher the data shown on the US plane. Resection margins may be able to be further improved with overlays from Diffusion Tensor Imaging (DTI) to show eloquent brain pathways. This method can be especially powerful if a contrast-enhanced MR volume is available.

1.2 Tumour Resection

Primary intracranial tumours occur relatively infrequently as compared to other cancers (4-11 cases per 100,000 people in the developed world¹²), but the rate of incidence has been steadily rising¹³.

For treatment, resection of the tumour is often necessary. Research has suggested a correlation between quality of intervention and care and the survival outcomes for patients¹⁴. In the context of the surgical resection of tumours, the primary limitation of surgical access is the avoidance of critical brain structures¹⁵. This challenge can be improved with information from functional imaging overlaid onto the preoperative image. Furthermore, the incorporation of intra-operative imaging, such as with ultrasound, allows for better localization of treatment and informs the surgeon of anatomical changes in the brain¹⁶⁻¹⁹.

1.3 Common Challenges

1.3.1 Registration Error and Brain Shift

A variety of technical issues combine to induce registration errors during neurosurgery independent of the method used to navigate the procedure.

At the very start of a procedure, the choice of imaging modality and its parameters can result in spatial distortions. As a modality, Magnetic Resonance Imaging (MRI) can occasionally generate images that have several millimeters of spatial distortion as a result of external magnetic or gradient field inhomogeneities²⁰, or air/bone-tissue interfaces²¹. As MRI-visible markers are usually placed on the periphery of the imaging volume, these can be prone to distortion due to magnetic field inhomogeneity in the bore.

After the pre-operative imaging is complete, the patient is prepped for surgery. Afterwards, he or she is often placed in a different orientation than when scanned. The MRI-visible markers used to locate the MRI volume in optical tracking space can move slightly at this point as a result of gravity affecting the skin differently. Finally, small amounts of brain shift may have occurred even before the surgery begins. These minor variations are corrected for in practice during radiotherapy sessions by registering the MRI to an intraoperative CT volume (though this is not available for conventional surgical procedures).

Once the surgery has started, the anatomical changes in the brain are exasperated after the craniotomy is made. Intracerebral landmarks can move up to a centimeter^{22,23}. The

major driver of this “brain shift” is the loss of tissue volume from the resection cavity, reduced cerebro-spinal fluid (CSF) pressure, and the force of gravity²³. Individually, these factors do not predict the entirety of brain shift²³. The consequences of brain shift can impede a surgeon’s capacity to delineate eloquent brain regions from diseased tissue and consequently affect decisions regarding resection radicality.

Brain shift correction is a major topic of research for medical imaging researchers. The majority of systems fuse some sort of intraoperative measurement along with some assumptions about the brain shift and the pre-operative image volume. The most rudimentary of corrections may take the form of a surgeon placing a pointer tool with a measured location on a landmark and manually translating the registration to try to improve the local accuracy of a registration.

1.3.2 Human Factors

Neurosurgical navigation and planning involve perception and cognition tasks that apply in various spatial frames of references. This means the surgeon is tasked with the mental fusion of an egocentric frame (with respect to the user), an environment frame (the operating room), a display frame (the display), and an object frame (the tracked tool)^{24,25}. Abhari et al.²⁵ studied the effects of various visualization methods on spatial reasoning tasks related to tumour resection and found a measurable difference in performance as a result of the visualization method used²⁵. The results can be extrapolated to come to the conclusion that a surgeon’s ability to identify and measure brain shift may be influenced by the choice of display, its location, and how visualizations are presented.

Navigated ultrasound reformats the preoperative image to match the view of the intra-operative ultrasound image. This, in principle, reduces the cognitive effort of the surgeon in mentally fusing the two co-ordinate frames.

1.3.3 Sterile Field / Reprocessing

Designing a system that supports effective reprocessing is a major consideration with any technology developed for surgery. Most of the hand-held tools end up falling in the “critical device” category of the Spaulding Classification as adopted by the FDA²⁶.

Ultrasound probes have specific additional guidance from the FDA in neuro applications. For example, ultrasound disinfectants can be pyrogenic, and consequently the probe must be thoroughly covered during a procedure²⁷.

1.4 Stereotactic Frame

The stereotactic frame is an essential component of image-guided neurosurgical procedures worldwide. There are many variants of the frame, but they all share three major functions:

- rigid fixation;
- adjustment and display of position; and
- mechanical guidance of surgical tools.

Stereotactic frames come in a variety of form factors, and may be invasively mounted, or non-invasively mounted²⁸. It may not be surprising that in the case of biopsies, using a frame instead of performing the biopsy freehand without navigation provides marked gains to patient outcomes²⁹.

One of the major drawbacks of this system is that there is limited visualization of the frame's co-ordinate system on the pre-operative image display. Therefore, when referring to the pre-operative volume, the surgeon has to do this transformation mentally with help from the imaging markers that are co-located on the patient and the volume. For live intra-operative visualization, one must use an additional modality with the frame such as fluoroscopy, ultrasound, intra-operative Magnetic Resonance Imaging (iMRI), or even magnetic/optical tracking.

The physical presence of the frame is both a blessing and curse. It provides a good physical guide for the instrument being used, but the frame itself is bulky, and occasionally a burden to fixate on the patient²⁹. The visual fusion of the mechanical device to the patient's head may help cue the surgeon against very large misregistrations, however. In addition, one may require a smaller room to perform frame-based surgery instead of a frameless surgery³⁰.

1.5 Frameless Stereotaxy

As an alternative, there are many commercial implementations of systems that allow for frameless neurosurgical navigation^{31–33}. These systems often consist of an optical tracking system combined with pre-operative or intra-operative images. Such neuronavigation systems comprise of a tracking system, computer, and a display that shows annotations to aid the surgeon with fusing the various co-ordinate systems together.

A typical frameless stereotaxy system has the following workflow:

- fiducial identification from MRI;
- pointer Calibration (optional);
- patient preparation / fixation;
- draping;
- registration using touchpoint fiducials and surgical tracked pointer; and
- resection with guidance of reformatted images.

Unfortunately, for some procedures and workflows, especially those related to targets in the deep brain, the accuracy offered by a frameless stereotaxy systems may not be enough, and the procedure requires the benefit of an intraoperative modality. In addition, there have been experiences documented that suggest that certain frameless stereotaxy systems may be systematically worse in terms of procedure time and accuracy³⁴.

There have also been systems that appear to be a hybrid between the frameless and framed stereotactic surgery systems. In these systems, a tracked mechanical arm provides a similar function, but without the burden of needing to be fixed to the patient during the pre-operative scan²⁹. The major technological leap with these systems is the presence of a monitor containing a surgical plan and/or pre-operative images that update with live image-feedback from the user. The live image feedback can show projected toolpaths and aid the surgeon in avoiding damaging eloquent regions when functional images are overlaid.

1.5.1 Optical Tracking Error in Frameless Stereotaxy

There is a certain amount of tracking error inherent in optical tracking systems. West et al.³⁵ provide theoretical bounds on the tracking error of tools based on the work of Fitzpatrick et al.³⁶, assuming a registration between the expected and measured marker locations. In practice, proprietary algorithms used in surgical navigation tracking systems produce better rigid-body tracking performance than that predicted by West et al., as presented by Wiles et al.³⁷

Passive marker-based systems have been shown to be immensely popular, though they come with a small accuracy penalty over actively tracked systems^{37,38}. From the standpoint of a medical devices designer, I can see them to be especially attractive over the active markers due to the easier electrical safety-testing requirements³⁹. Sterilization and biocompatibility (per ISO 10993⁴⁰) validation is also easier by virtue of having fewer parts and no disassembly. Unfortunately, these benefits come with the major drawback of marker degradation and partial occlusion of the markers. The markers get damaged by blood, other fluids, and/or incidental contact with hard and/or sharp objects such as surgical tools. To my knowledge, the effects of marker damage on system-level accuracy have not been publically studied, though my expectation is that the effects are not insignificant. Partial occlusions can be mitigated with user-training and informed assumptions on the part of the designer, but can be unavoidable depending on the context. The designer may choose to cull poses that are prone to partial occlusions by defining a marker-normal or face-normal constraint. Thus, there is a compromise between tracking accuracy and line-of-sight when such constraints must be used.

As a result of the trade-offs between reprocessing, tool-life, ergonomics, cost, and accuracy, manufacturers choose different accuracy set-points in their various surgical navigation systems. Nonetheless, there exists no published data about the system accuracy between various neurosurgical navigation systems²⁸.

Table 1: Summary of image modalities available for intraoperative guidance

| Intraoperative Modality | Access Via | Image Characteristics | Tool Localization via | Examples |
|--------------------------------|---------------------------------------|--|------------------------------|---|
| Intraoperative MRI | No access needed | Good Soft Tissue Contrast, Functional Information | Image / Tracker / MRI-based | Brainlab iMRI, Polestar iMRI, Visius IMRI (IMRIS) |
| Intraoperative CT | No access needed | Bone structure visualization, localization of metal tools | Image / Tracker | Ubiquitous CT scanners |
| Pathology Samples | Resection Cavity | Microstructure, individual cells | Visual Inspection / Tracker | |
| Portable Fluoroscopy | No access needed | Bone structure visualization, localization of metal tools | Image / Tracker | Ubiquitous portable C-Arm systems |
| Intraoperative US | Craniotomy / Burr Hole | Good soft tissue contrast | Image / Tracker | Ubiquitous ultrasound systems + convex array transducers, BK Medical US with burr-hole transducer |
| Cannula + Optics | Craniotomy | Minimally invasive optical visualization of resection cavity | Microscope / Tracker | Nico Brainpath |
| Endoscope | Burr hole / Nasal Access / Craniotomy | Minimally invasive optical visualization of | Image / Tracker | Ubiquitous surgical endoscopes |
| Exoscope | Craniotomy | Excellent | Tracker | Synaptive Medical Drive |
| Microscope | Craniotomy / Burr hole | Good | Optics / Tracker | Surgiscope Brainlab Flyer Carl Zeiss |

Increasing Interactivity →

1.6 Intraoperative Imaging

A number of neurosurgical procedures rely on intraoperative images for guidance. I have summarized some of the considerations for each modality in Table 1.

These intra-operative imaging modalities provide the surgeon with valuable navigation information, and can even augment frameless or framed stereotaxy. While the benefit of being able to directly view tools and the region of interest is great, workflow issues arise with the inclusion of intra-operative imaging.

The modern neurosurgical operating room has access to more medical imaging modalities than ever before. Each image modality has a role to play in informing the surgeon as to where to go to conduct a given procedure. The use of intraoperative MRI (iMRI) has been discussed in the literature at length with experiences from systems such as those developed by Medtronic and iMRIS⁴¹ indicating a possibility for improved patient outcomes⁴². However, these systems are very expensive, require a great deal of technical expertise and planning, and increase operating time¹⁷. This is unfortunate, as MRI offers outstanding soft-tissue contrast, as well as invaluable functional information that can be used to inform the live surgery.

1.7 Ultrasound in Neurosurgery

Where MRI's use is almost exclusively pre-operative, ultrasound is used almost exclusively intra-operatively, due to the need for a craniotomy. Like MRI, ultrasound offers good soft-tissue contrast, but is more difficult to interpret.

Intraoperative Ultrasound (iUS) is an alternative to iMRI that may have comparable gains to patient outcomes without the significant costs^{5,6,43-47}. By utilizing iUS during a neurosurgery session, it is possible to account for the apparent movement and deformation of the anatomy as well as calibration issues in the neuronavigation equipment.

While ultrasound has a long history of use in neurosurgical applications dating back to the 1950s using A-mode US images⁴⁸, it currently is not a dominant modality. One reason for this may be that there are a great deal of considerations to take into account for

effective US imaging. These issues include patient-positioning, resection planning, selection of retraction tools, the management of bleeding, and resection approach, and relate to acoustic coupling, and reducing US image artefacts⁴⁸⁻⁵¹. Another caveat of US usage in neurosurgery is that its interpretation benefits greatly from the context provided by a reformatted or annotated pre-operative image showing the corresponding region of interest. Finally, ultrasound's lack of appeal is partly due to the fact that surgeons are not as familiar with it⁵².

There are now a variety of state-of-the-art systems that allow for the fusion of intraoperative ultrasound with pre-operative images, displaying on-screen visualization of procedures in progress¹⁻⁴. In doing so, US images can be employed as a template to which pre-operative images can be registered, to correct for brain-shift, to provide live-image feedback, and consequently to improve confidence when making resection margin decisions near eloquent regions during tumour surgery^{1,5,6}. These systems often make use of infra-red camera-based tracking systems that estimate the pose of hand-held tools and imaging probes to present helpful interpretive visualizations. As can be surmised from Table 1, optically-tracked freehand ultrasound implementations are limited by line-of-sight issues, bulkiness of optical tracking tools, cost, maintenance of the sterile field, and space constraints in the neurosurgical operating room^{30,53,54}. Despite the many advances in commercial and research systems, ultrasound continues to be underutilized.

It is my view that existing navigated ultrasound systems may have missed the appropriate balance between workflow changes and features. A medical device company has a tough choice between providing a solution that is agnostic to existing hardware that a hospital already owns and is familiar with (e.g., an ultrasound system), or offering a solution that is specific to a combination of hardware with tighter integration, but with potentially a higher capital/training/infrastructure cost to the hospital requiring it to support another vendor's system. The system-agnostic workflow can clutter the operating room space with a great deal of equipment (Figure 3).

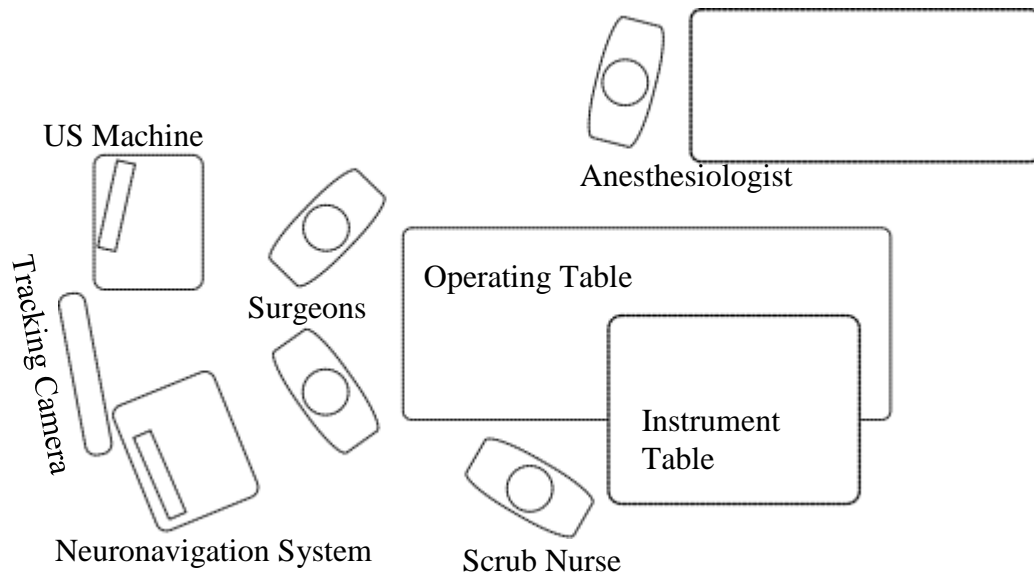


Figure 3: Conventional tracked ultrasound operating room layout

An ultrasound agnostic multi-modal imaging system makes compromises with the ultrasound tracker calibration. Usually they require a calibration step before the ultrasound probe is draped. The risk assessment activities conducted by a medical device designer seeking to make a navigated ultrasound product may lead them to classifying the calibration hardware as sterile. An alternative to calibration hardware explored by recent research may be in-situ calibration⁵⁵, where a tracked surgical tool is placed inside the ultrasound FOV to compute its calibration.

The burden of optical hardware required for an ultrasound agnostic system, in addition to a tracking camera, may include

- an ultrasound probe “clamp” or fixation device to hold the optically tracked sensor (under the ultrasound cover);
- a tracked rigid body for holding the optical markers allowing for the ultrasound cover in between the rigid body and the above device without puncturing it; and/or
- a calibration device or tool.

As mentioned in 1.3.3, most of this hardware is likely to be classified as “critical devices” and become part of the hospital’s reprocessing workflow. From personal experience, an attempt to duplicate the arrangement described by Mercier et al., where the spherical optically-tracked markers were snapped onto their posts overtop of the ultrasound cover⁵⁶, resulted in the observation that the fit of the spheres to their posts was often compromised. This experience is limited to the ultrasound cover being used, as well as to the optical tracking post/marker combination. Consequently, while that arrangement has the advantage of reducing the hardware required, it may not be appropriate for a commercial product.

Regardless of the aforementioned choice regarding ultrasound vendor independence, an optically-tracked ultrasound probe may further burden the ergonomics in a task already fraught with repetitive strain injury⁵⁷. One study found that up to 90% of sonographers are imaging with some amount of pain⁵⁸. Though in a neuro-imaging context the throughput would be much smaller, this statistic speaks to the importance of not making the use-case worse. Since the optical tracking marker arrangements often fall right on the natural gripping points of the probe, add weight, and create line-of-sight constraints, there is reason for concern. Even without navigated ultrasound, maintaining line of sight in a frameless stereotaxy system is a major challenge⁵⁹. The line-of-sight issues may be further exasperated by the presence of viscous acoustic coupling mediums in the surgical field, and fluids on the ultrasound probe cable migrating onto the retro-reflective surfaces of the optical markers, thus compromising accuracy. The wider the desired field-of-view and accuracy (i.e., size) of the tracked tool, the greater the chance of intrusion by the cable or impact during the session. Advocates of optical tracking reason that these issues can be designed around though I have yet to find a compromise that makes for a truly positive experience. Due to the risk of IR interference between cameras of multiple systems, optically tracked ultrasound solutions mandate some level of integration with the neuronavigation system. Currently available solutions do not incorporate any workflows that work around a stereotactic frame.

1.7.1 Ultrasound Imaging Considerations

The literature documents a few different scenarios for typical ultrasound use, which are summarized in the following sections.

1.7.1.1 Pre-Resection Imaging

Prior to the resection cavity being made, the ultrasound probe can be used as a quick check on the craniotomy location and size. Acoustic coupling may be performed with the use of a saline filled sterile bag. As a standoff, this can help bring more of the ROI into the field of view of the US probe depending on its location.

1.7.1.2 Intra-Resection Imaging

Ultrasound probes can image within the resection cavity by flushing it with saline or another coupling medium. This usually requires planning in advance to ensure that the resection cavity is oriented with gravity. Alternatively, some surgeons have documented the creative use of bone-wax in making “dams” so that the coupling medium can stay in place and allow for ultrasound imaging⁶⁰. Knowledge of common ultrasound imaging artefacts benefits its use significantly. The most common artefact is the acoustic enhancement artefact that arises from the sound waves being more attenuated outside the saline filled cavity than within the cavity. Consequently, the area in which the surgeon is most interested (the bottom of the resection cavity) unfortunately shows up as hyper-echoic. The saline itself shows up with bubbles in the cavity, which can be used to better distinguish it from tissue⁵⁰. Unfortunately, most intra-resection ultrasound imaging impedes the use of surgical optics, another key intra-operative imaging modality, unless a second craniotomy site is made. Though it comes with significant drawbacks, making a second craniotomy site also has the benefit of reducing the effects of the acoustic enhancement artefact.

Another way to avoid the acoustic enhancement artefact and filling the resection cavity with saline is to use a miniature ultrasound probe. Coburger et al.⁴⁷ found this method to be a powerful way to differentiate cancerous tissue, with marked gains over imaging from the top of the resection cavity.

A final, essential consideration, is that as the surgery continues, bleeding tends to make the tumour contrast worse.⁵²

As described by Prada et al.⁵², typically brain structures show up as follows when visualized using ultrasound:

Table 2: Neurosurgical ultrasound semieology per Prada et al.

| | |
|------------------------|---|
| Hyperechoic Structures | “...skull, Vessels wall, choroid plexuses, arachnoidal folds, ependymal, dural fold, brain-lesion interface” ⁵² in addition to blood clots, and calcifications |
| Hypoechoic Structures | “Cerebrospinal fluid, ventricles, connective fibres” ⁵² |
| Isoechoic Structures | Brain parenchyma |

There is also the ability to use transcranial ultrasound to develop an understanding of the ROI. Unlike iUS, transcranial ultrasound is done with a low frequency US probe (<2Mhz) through the temporal bone. This arrangement results in poorer soft-tissue contrast, though it is sufficient for a variety of diagnostic tasks^{61,62}. Recent research has shown potential in *ex vivo* tissue for transcranial ultrasound to correct for brain-shift, though it has yet to be pursued in a clinical context⁶³.

1.8 System Design

Considering the above challenges, the objective of the work presented in this thesis is to improve the state-of-the-art of tracked ultrasound systems by incorporating the following features:

- free from calibration, or with minimal calibration;
- free of manual registration, or robust to large registration errors;
- independent of surgical navigation system;
- independent of ultrasound imaging hardware;

- less sensitive to line-of-sight issues;
- minimal hardware to reprocess;
- can be an optional adjunct to optical tracking;
- pre-resection workflow; and
- brain shift visualization.

This work addresses a different subset of tracked ultrasound problems than those that recent research systems attempt to solve, in that it aims to develop a system that supports a workflow early in the procedure, prior to the resection cavity. In this situation, ultrasound can form a sanity check on the craniotomy location⁶⁴ and registration, inform the surgeon of anatomical changes⁶⁴, and provide meaningful data on tumour echogenicity. This can form an essential component in maintaining a minimal craniotomy, verifying that an approach is free of important vasculature, and also guiding a trocar during a minimally invasive approach. Even at this point in the procedure, according to Coburger et al.⁶⁴, ultrasound informs the surgery more reliably than the surgical navigation system, and can provide marked gains to the productivity of the surgeon by “gaining a confident idea of the surrounding structures.”

The system must be designed in the context of anticipated advances in consumer electronics technology. In particular, with major technological companies investing significant effort to develop the integration of a variety of inexpensive sensors with simultaneous localization and mapping (SLAM) algorithms, it is only a matter of time before these kinds of systems find their way into surgical image-guidance. Thus, whereas today’s neuro-navigation systems employ a single very accurate tracking system, the future of image guidance may feature systems that integrate measurements from a heterogeneous assortment of sensors to perform localization of tools.

My approach is therefore to develop an alternative way of constraining the multi-modal registration to produce an intra-operative guidance system that incorporates a multi-modal image registration algorithm, craniotomy site definition, sensor data, and the motion model as components in my system. To my knowledge, this has not been done before.

A key component of this system will be a fast and effective 2D-3D multimodal registration. A 2D-3D registration will enable a Kalman-filtering based algorithm to treat individual ultrasound frames like sensor positioning data in a way similar to commonly used in SLAM (Simultaneous Localization and Mapping) algorithms.

The system that this thesis strives to achieve is in a pre-resection workflow in light of the serious workflow impediments that intra-resection ultrasound presents (i.e., challenging acoustic coupling and acoustic artefacts that reduce the specificity of intraoperative ultrasound during surgery⁶⁵). Nonetheless, the output of this system may feed into a monomodal volumetric brain-shift correction algorithm in future work.

1.9 Image-Based Registration

One of the key themes of the work in this thesis is image-based registration. In medical applications, the most common form of image-based registration is volumetric. Registration can be divided into two sub-algorithms: a similarity metric and the optimizer. The similarity metric serves the purpose of a cost function – given two images, it produces a number corresponding to two images’ similarity (Figure 4). The optimizer’s function is to produce a transform to reformat the “moving image” to produce an output that is most similar to the “fixed image” using the output of the similarity metric. Consequently, the similarity metric is usually evaluated many times until the optimizer converges on an optimal transform for the moving image.

For example, in the case of this thesis, where a 2D-3D US-MRI registration is evaluated, the MRI is the moving image, and the ultrasound is the fixed image. The optimizer perturbs the MRI image transform until it matches the location of the ultrasound probe.

The simplest of similarity metrics is the sum of absolute differences (SAD), the sum of absolute differences between corresponding pixels between the images. The sum of squared differences (SSD), similar to SAD, is the sum of squared differences of pixel intensities, but features a steeper slope for better optimizer convergence. SSD divided by the number of pixels becomes the mean-squared-error (MSE) metric, resulting in a number

that is easier to compare between image sets. Unfortunately, these metrics suffer once the images are even slightly different in pixel intensities, i.e., when they have slightly different contrast or brightness values, or have varying degrees of overlap. Normalizing the image intensities makes these metrics more robust to contrast/brightness values. Normalized Cross Correlation (NCC) does just this, demeaning, and normalizing the images with their respective ranges. (Essentially, becoming the dot product of the normalized images.)

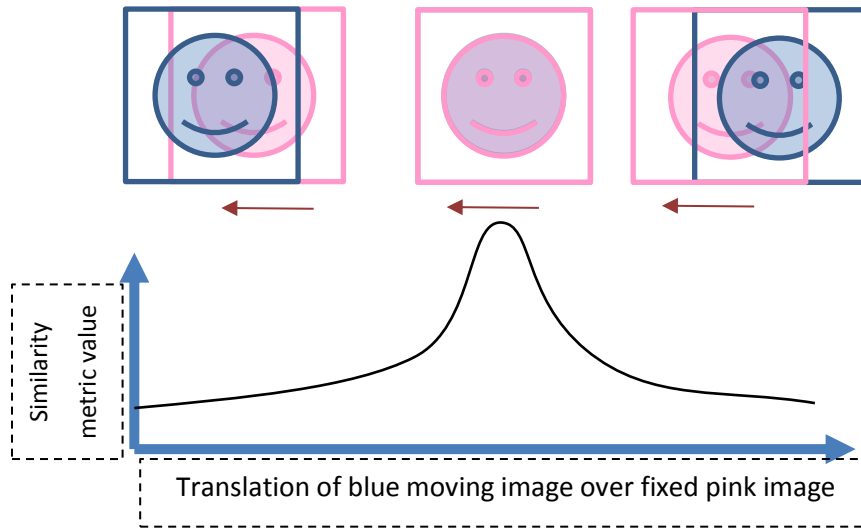


Figure 4: Registration similarity metric function

Images generated from fundamentally physical processes still suffer with the above intensity-based metrics, since pixels in one modality may consistently map differently to pixels in another. Two of the most established similarity metrics for multimodal registration are Mutual Information⁶⁶ and the Correlation Ratio⁶⁷.

Mutual Information (MI) is simply explained as how well a statistical relationship formed by the intensities of two images area predict the values of one image from another. The variants of mutual information act to reduce the effects of heavy noise, incorporate some aspect of the image-formation, or varying relationships between the two images (as is especially the case with ultrasound).

Correlation Ratio (CR), like MI, is related to the statistics of the image-intensities between two images, but is not as computationally challenging to compute, and is less sensitive to the number of pixels being compared. Roche et al. present it in an ultrasound

application by incorporating the MR image gradient, image intensities, and the ultrasound image intensities⁶⁸. CR simplifies to another famous similarity metric, NCC, when the relationship between image intensities is linear.

There is also another class of similarity metrics grounded in the notion of local self-similarity. Such metrics compare an abstraction of the input images. For example, the Modality Independent Neighborhood Descriptor (MIND) multi-modal registration metric has been successfully applied to a variety of registration scenarios⁶⁹ including US/MRI registration⁷⁰.

1.9.1 Multimodal US/MRI Image Based Registration in Neurosurgery

Multi-modal registration between ultrasound and MRI using optical tracking for the purpose of brain-shift correction has been a topic of research for decades now^{18,71}. In the context of US/MRI registration, much work has been done since the release of the Brain Images for Tumour Evaluation Database (BITE)⁵⁶, which provides the ability to validate new similarity metrics. The list of similarity metrics validated on the dataset is long, including LC2^{72,73}, GOA⁷⁴, COCOMI⁷⁵, SESAMI⁷⁶, RAPTOR⁷⁷, and miLBP⁷⁸. In addition, there has been work creating volumetric pseudo-US images from a segmented MRI volume^{79,80}.

These algorithms have not been used to place individual 2D US slices within the space of a 3D MR image in the manner described in this thesis, though the LC2 algorithm's introductory paper displays results for the unreconstructed US data⁷², unlike the other available work^{74-78,81,82}. This model of registration is compelling, as it makes the step of gridding the ultrasound voxels unnecessary.

These similarity metrics developed in the context of US/MR registration, especially when used for brain shift correction, are often used in some kind of deformable registration framework. In a deformable registration, the spatial location of individual pixels is free to move per some defined function within some constraints.

Optical tracking error can be significant when propagated to a point in the ultrasound field of view. When placed in a grid, the diffeomorphic constraints that are applied on algorithms acting on these volumes are violated. A model that takes into account optical tracking errors may be better able to place these slices. None of the prior work incorporates these models to aid the registration.

The lack of published data for 2D to 3D registration of individual slices is unfortunate, as there has been excellent work showing how a graph-based deformable registration can do both slice localization and in-plane slice deformation given a small search space. In these experiments, Ferrante et al.^{83,84} used six sets of ten slices from one of the patients in the BITE database, and utilized the first slice's optical tracking pose as an initialization for the following slices. It is possible that this method may have potential to work with larger search spaces and with longer series of slices with the use of a more sophisticated similarity measure.

In a monomodal context, there is notable work on 2D-3D Ultrasound slice-volume registration for prostate images. De Silva et al.^{85,86} employ normalized cross correlation to refine the pose of a 2D US probe given an existing 3D US volume. Also notable are attempts to create real-time tracking of the US probe using 2D-3D registration⁸⁷. Image-based 3D-3D monomodal registration is involved with the Koelis Urostation Touch⁸⁸, allowing for image-based ultrasound navigation.

1.10 Other Pose Estimation methods

There are methods other than registration or optical tracking that have been used to develop a pose estimation for ultrasound probes. For example, out-of-plane probe movement can be partially derived from US speckle decorrelation models⁸⁹⁻⁹¹. Recent developments have shown that it may be plausible to help constrain an ultrasound probe's pose in *in vivo* tissue⁹²⁻⁹⁴, but these algorithms rely on obtaining the underlying radio-frequency (RF) data from the ultrasound probe instead of the fully processed B-mode images. Other researchers have worked to develop a pose-estimation system without RF data while incorporating visual-servoing, but these efforts have been unable to produce similar accuracy⁹⁵⁻⁹⁷. It may nonetheless be plausible to incorporate pose-information from

these algorithms into the kind of multi-sensor fusion system I am working on to help constrain the registration of a 2D ultrasound probe's pose.

1.10.1 Sensor/Data fusion with Kalman Filtering

The use of multi-sensor data fusion for the computer guidance of freehand tools has been described in the literature a number of times. For example, this model has been used as a way to improve the accuracy of speckle tracking with inertial measurements⁹⁸, to create optical-inertial hybrid tracking systems⁹⁹, or to use both electromagnetic and optical tracking¹⁰⁰ to support a given procedure. Of special interest to me is work that has been done to combine speckle tracking with multi-modal registration with spine images¹⁰¹, which showed a good deal of success with CT-US registration combined with speckle-tracking in a spine phantom and in a lamb spine. The work presented in this thesis demonstrates how these kinds of powerful sensor-fusion frameworks can be applied in a neuro-navigation context when a 2D/3D similarity measure is incorporated.

Many of the aforementioned sensor fusion systems employ Kalman Filtering. All measurements have some uncertainty associated with them, and thus a process that I seek to observe is unknowable past a certain threshold of accuracy. Furthermore, the knowledge, or “belief” in the state of the system will change with the passing of time as a result of the system's model dynamics. Thus, such systems can be represented as a Markov chain where the current state of the system $x(t)$ is measured indirectly through measurements $y(t)$ (Figure 5).

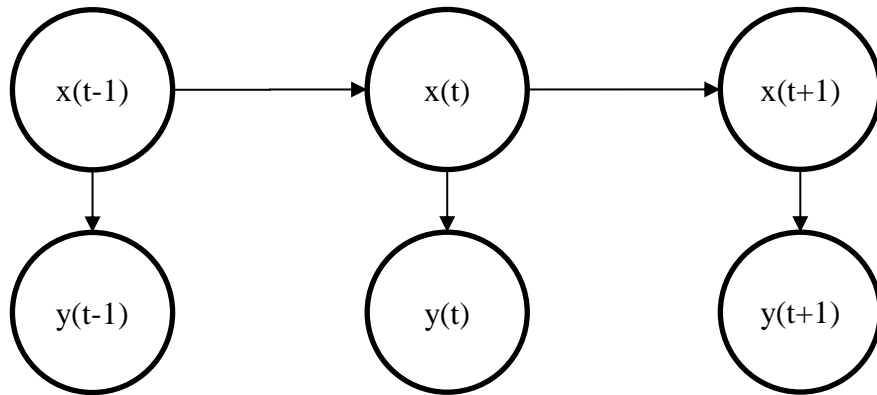


Figure 5: Hidden Markov Model representation of the evolution of states ($x(t)$) and their measurements ($y(t)$) in a pose measurement and estimation problem

The classic implementation of an algorithm that relies on the above model is the Kalman Filter, which represents a special case of a Markov chain, where measurements combined with the state transition function produce estimates of the tracked object's pose. In this framework, Gaussian distributions represent the belief of the state of the object and the measurements. As shown in Figure 6, a measurement update step refines the *a priori* (before the measurement) belief, resulting in the *a posteriori* (after the measurement) state belief. Before the next measurement, a prediction step creates the next *a priori* belief, which, in general, is less certain than the previous *a posteriori* belief. How much the *a posteriori* state estimate incorporates measurement is determined by the “Kalman Gain” matrix, which is a function of the measurement model and its error covariance. The prediction step is informed by the state transition function, and the state transition

covariance. The recursive nature of the Kalman Filter is made explicit in Figure 6.

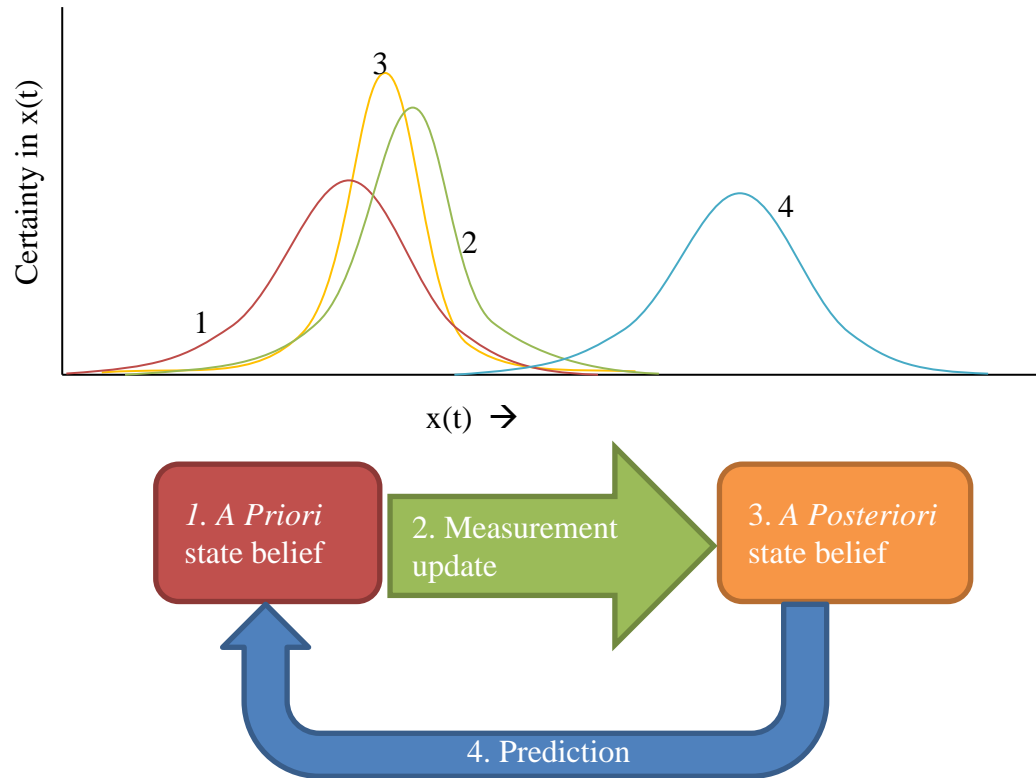


Figure 6: Kalman filter algorithm steps

In pseudo-code form, the algorithm appears as follows (adapted from Thrun et al.¹⁰², excluding control inputs) in Figure 7.

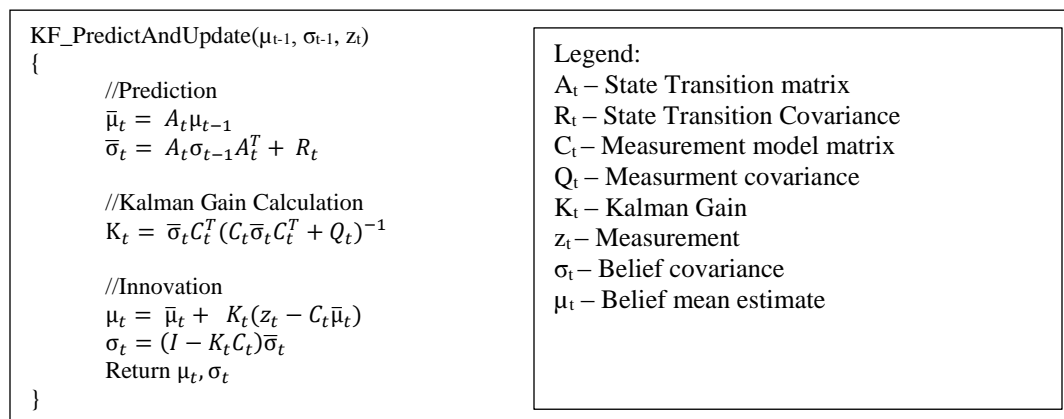


Figure 7: Example Kalman filtering pseudocode

1.11 Summary

My work in this thesis comprises the following novel contributions:

- exploration of the applicability of LC2 in the context of 2D-3D US-MRI registration using the Brain Images for Tumour Evaluation Database;
- development of a new similarity metric based on LC2 called BOXLC2 (this metric has a faster GPU implementation by virtue of requiring fewer steps to compute; I show this to be approximately equivalent to LC2 in terms of speed); and
- demonstration of a 2D/3D image similarity metric inside an Unscented Kalman-Filter (UKF) framework fusing the registration algorithm with noisy sensor measurements from an inertial measurement unit (IMU).

Given the goals mentioned in section 1.8, the UKF algorithm will attempt to

- perform LOS correction when performing optically navigated ultrasound procedures; and
- be a standalone ultrasound navigation system that meets the requirements set out in section 1.9 when combined with an inertial measurement unit.

Chapter 2

2 2D/3D US – MRI Slice to Volume Registration

2.1 Background

The existing work on US-MRI slice-to-volume registration is limited, as there is no unanimously accepted approach to the challenge¹⁰³. There has, however, been much work in US slice-to-volume registration in a single-modality context⁸⁵, as well as with US to other modalities^{84,104}.

Wein et al.¹⁰⁵ introduced the LC2 similarity metric for the purpose of abdominal US-CT registration, as well as a patchwise variant for US-MRI⁷². The metric was further expanded upon by Fuerst et al.⁷³ For the sake of simplicity, we will refer to the patchwise variant presented by Fuerst et al.⁷³ Unlike most prior work, which performed a US volume reconstruction step to do a volume-volume registration, the LC2 Metric has been validated in a multi-slice to volume registration context. This work also included results for registration with a sparse collection of slices.

As presented in Wein et al.⁷², for a given patch Ψ at location x_i in image Ω , LC2 tries to fit an US slice $f(\Psi, x_i)$ to an MRI slice, as a linear function of the MRI image intensities, $p(x_i)$, and gradient magnitude $g(x_i)$ using the following formula:

$$f(\Psi, x_i) = \alpha p(x_i) + \beta g(x_i) + \gamma \quad (1)$$

where α , β , and γ are solved for each patch by minimizing the difference between $f(\Psi, x_i)$ and $u(x_i)$ intensities for each voxel-wise patch using least-squares fitting. The LC2 similarity metric is:

$$S = \frac{\sum_{\Psi \in \Omega} \left(1 - \frac{\sum_{x_i \in \Psi} |u(x_i) - f(\Psi, x_i)|^2}{|\Psi| \text{Var}(u(x_i) | x_i \in \Psi)} \right)}{\sum_{\Psi \in \Omega} (\text{Var}(u(x_i) | x_i \in \Psi))} \quad (2)$$

As described by Wein et al.⁷², the denominator of the similarity function serves to attenuate regions with acoustic shadowing (just as it did in the CR similarity metric).

2.2 Methods

2.2.1 Overview

I have developed a PyCUDA enabled Python module in 3D Slicer¹⁰⁶ to explore US Slice to MRI volume registration. The software has an implementation of the LC2 metric, as well as a variant that I have developed to aid with improving computation time. The module can create virtual craniotomy sites from a given pose and then search for the best possible pose within those craniotomy sites in 3 degrees-of-freedom (3DOF), reusing the orientation pose components from MNI’s Brain Images for Tumour Evaluation (BITE) data, or in 6 degrees-of-freedom (6DOF).

2.2.2 GPU LC2 Implementation

My implementation is partially derived from the example MATLAB code¹⁰⁷ in addition to the published work on LC2⁷³. For the gradient computation, I employed the Scharr operator¹⁰⁸ in the vertical direction only, since the computation of other gradient components had no effect on the registration. Arguably, my implementation is more consistent with the physics of US image formation.

The example MATLAB code also has some additional caveats not mentioned in the original publications in that the MATLAB implementation does not compute the pixel-wise similarity for patches that have a majority of nonzero pixels, or if the ultrasound image variance is zero. This feature enhances the stability of the registration metric, by ensuring that there are enough pixels to compute the $f(\Psi, x_i)$ term.

Finally, as a deviation from the published work and the example MATLAB code, I chose to skip the accumulation of pixels that correspond to zero-values in the US image, providing a significant speed improvement without degrading the registration metric. Pseudocode for my implementation is shown in Figure 8.

In my experiments, re-slicing, gradient computation, and US patch weightings are computed in a different kernel or on the computer’s central processing unit (CPU).

```

LC2_Kernel(USImg, ReslicedMRIImg, ReslicedMRIGradImg)
{
    For each pixel in this patch's columns:
    {
        Copy data from USImg, ReslicedMRIImg and ReslicedMRIImg into shared memory
        Synchronize Kernels
        For each pixel in this patch's rows
        {
            If the US image intensity is > 0, accumulate intensities for solving LC2 Coefficients from
            shared memory
        }
    }
    Return early if most of this US image patch is zero.
    Solve for LC2 coefficients from accumulated intensity values.
    For each pixel in this patch's columns:
    {
        Copy data from USImg, ReslicedMRIImg and ReslicedMRIImg into shared memory.
        Synchronize Kernels
        For each pixel in this patch's rows
        {
            Accumulate the difference between the LC2 function and US pixel intensity
        }
    }
    Similarity = Sum of differences between LC2 function and US pixel intensity divided by the US
    image variance divided by the number of pixels
}

```

Figure 8: Pseudocode for LC2 GPU kernel

2.2.3 Boxcar Filter Normalized LC2 (BOXLC2)

As the $|u(x_i) - f(\Psi, x_i)|$ term in the numerator of equation 2 requires an additional memory access of complexity $O(n^2)$ with the patchsize after already traversing the pixels in the patch to compute $f(\Psi, x_i)$, there may be room to improve the computational efficiency without affecting accuracy. By removing this expensive memory access, and replacing it with another measure of the metric's fit, I can potentially improve the metric's speed.

Boxcar Filter Normalized LC2 (BOXLC2) posits that the US image-generated voxelwise by $f(\Psi, x_i)$ will resemble an US image where each pixel is the mean of the pixels in the input patch when the registration is poor (otherwise known as a boxcar filtered image). Consider the situation where a patch of ultrasound data is fitted to a patch of noise of the same size. Solving for eq. 1, $f(\Psi, x_i)$ would give the average ultrasound intensity, $\overline{u(x_i)}$ of the patch centered at a given x_i , as that is the best fit that can be found for uncorrelated noise. As the desired MRI slice should perform better locally than

uncorrelated noise, one can see how $f(\Psi, x_i)$ would move towards $u(x_i)$ from $\overline{u(x_i)}$. Therefore, a normalized dissimilarity measure is formed by dividing $f(\Psi, x_i) - u(x_i)$ by $\overline{u(x_i)} - u(x_i)$. As a similarity metric, it thus takes the form of:

$$S(u) = 1 - \sum_{x_i \in \Omega} \left| \frac{f(\Psi, x_i) - u(x_i)}{\overline{u(x_i)} - u(x_i)} \right|, \text{ where } \Psi \text{ is a patch centered on } x_i \quad (3)$$

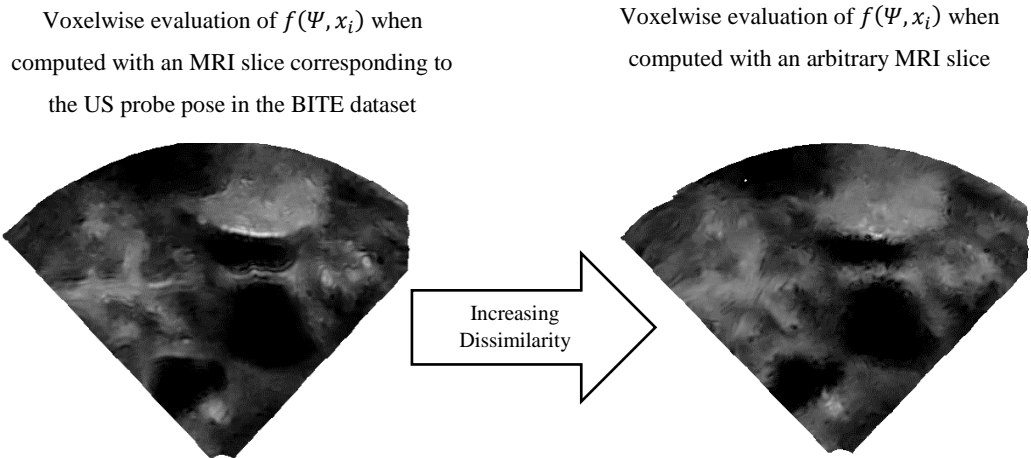


Figure 9: The voxelwise evaluation of $f(\Psi, x_i)$ creates simulated ultrasound image that resemble boxcar filtered US image as image dissimilarity increases

Pseudocode for BOXLC2 is shown in Figure 10.

```

BOXLC2_Kernel(USImg, ReslicedMRIImg, ReslicedMRIGradImg)
{
  For each pixel in this patch's columns:
  {
    Copy data from USImg, ReslicedMRIImg and ReslicedMRIImg into shared memory.
    Synchronize Kernels
    For each pixel in this patch's rows
    {
      If the US image intensity is > 0, accumulate intensities for solving LC2 Coefficients
    }
  }
  Calculate pixel-wise weight as the ultrasound pixel intensity minus the average US pixel intensity
  If the number of nonzero pixels in this patch is smaller than half the patch area, return
  Solve for LC2 coefficients from accumulated intensity values.
  Solve for similarity as the LC2 function evaluated at this pixel minus the US pixel intensity
  clamping the output value to a range of zero to one
}

```

Figure 10: Pseudocode for BOXLC2 GPU kernel

2.2.4 Particle Swarm Optimizer

I have implemented a stochastic optimizer known as a particle swarm optimizer¹⁰⁹. In this optimization technique's canonical form (inspired by the behaviours of social animals searching for a common goal), a "swarm" of particles represented by a vector of length N search through an N dimensional objective function search space, with attraction to the swarm's best value, and each particle's respective previous best value (Figure 11). The optimizer has been used in a wide variety of applications ranging from tuning algorithms such as neural networks, electrical grid optimization, biological system modelling, and robot path planning¹¹⁰. One of the attractive features of this optimizer is that it doesn't require the derivative of the objective cost function, since its maxima can often be narrow, and easily missed by a conventional gradient based optimizer. My implementation, based on the pyswarm library¹¹¹, is true to the original description presented by Eberhardt et al.¹⁰⁹, with the caveat that when a particle passes a constraint, it gets randomly placed in the search space with memory of its previous best location.

```

PSO_Iteration (particles )
{
    f = similarityfunction(particles)
    gbest = best particle in f
    For each particle:
        Store the best historical particle position in pbest[particle]
        v_particle =  $\Omega$  v[particle] +  $\Phi_p \times \text{rand}() \times (\text{pbest} - \text{particle\_position})$  +  $\Phi_g \times (\text{gbest} - \text{particle\_position})$ 
        particle_position = particle_position + v_particle
        If particle is outside bounds:
            reinitialize particle within bounds
}

```

Figure 11: Particle swarm iteration pseudo-code

The behaviour of the particle swarm is affected by constants Ω , Φ_p and Φ_g , where Ω determines the momentum of particles, and the Φ_p and Φ_g terms weight the influences of local and global best evaluations respectively. I chose a small Ω value of 0.15 to keep the particles within the search space, g and p values of 0.5, with the exception of the orientation component aligned with depth axis of the US probe, which I set at 0.3. I chose a swarm size of 30,000 particles, with an iteration limit of 50 and without any other

stopping criteria, taking advantage of the massively parallel computation abilities of the GPU to mitigate the risk of missing a maxima.

2.3 Testing Approach

To test the slice-based registration performance, I made use of the BITE database⁵⁶. Group 2 of the dataset comprises 14 cases with tracked pre-resection US slices, pre-surgical T1-weighted contrast-enhanced MRI volumes, and expert-identified homologous landmarks in both modalities.

To computationally constrain the problem, for each US probe pose I simulated small craniotomy sites (2cm x 2cm x 2cm) based on the original pose information and the skull-stripped brain surface. This approach was chosen to mirror clinical practice, where the craniotomy size is influenced by tumour size, and also to shrink the objective function search space for quick evaluation.

To create the craniotomy site, I employed the Brain Extraction Tool (BET) from the FSL neuroimaging pipeline¹¹² to get an estimate of the dural surface. I expect some error in the dural surface with the default settings, but since my search space has to be widened to accommodate for brain-shift, dural segmentation errors will not be consequential.

Using the distance between expert-identified homologous landmarks in both modalities, one can determine a target registration error (TRE). A caveat is that these landmarks were identified in reconstructed US volumes, and thus I execute this algorithm on the 2D US slice that is closest to each landmark.

Since the US slices included in these tests require them to be within 0.3mm of an expert-identified landmark in the reconstructed US volume, some of the landmarks are culled out of the BITE dataset. In addition, if during processing multiple targets appear in the same US slice, only the landmark that is closest to the original US slice's imaging plane is used. For the remainder of this paper, I shall refer to these as slice-target pairs.

Thus, I have selected 329 slices from the original 392. The mean TRE is 4.1mm for this set of target-slice pairs. This set of US slices forms the basis of my testing when I report TRE values. Figure 12 shows a histogram of errors for target-slice pairs that correspond to TRE values less than 5mm is shown in.

Both image-similarity metrics are operated on the MRI volume masked by the US image field-of-view. It is also pertinent to mention that voxels that fall outside of the brain-mask generated by FSL-BET are also removed from the computation.

Table 3: Slice-target pairs used in my experiments

| Patient Number | 1 | 2 | 3 | 4 | 5 | 6 | 7 | 8 | 9 | 10 | 11 | 12 | 13 | 14 |
|-----------------------------------|-----|-----|-----|-----|-----|-----|-----|-----|-----|----|-----|-----|-----|-----|
| No. of Landmarks in BITE Database | 37 | 35 | 40 | 32 | 31 | 37 | 19 | 23 | 21 | 25 | 25 | 21 | 23 | 23 |
| Mean initial TRE (mm) | 4.9 | 6.5 | 9.4 | 3.9 | 2.6 | 2.3 | 3 | 3.6 | 5.1 | 3 | 1.5 | 3.7 | 5.1 | 3.8 |
| No. of Landmarks in test subset | 32 | 30 | 13 | 29 | 28 | 35 | 15 | 22 | 19 | 20 | 24 | 19 | 21 | 22 |
| Mean TRE in test subset (mm) | 5.3 | 6.3 | 9.7 | 4 | 2.6 | 2.3 | 4.3 | 3.9 | 4.9 | 3 | 1.5 | 3.7 | 5 | 3.8 |

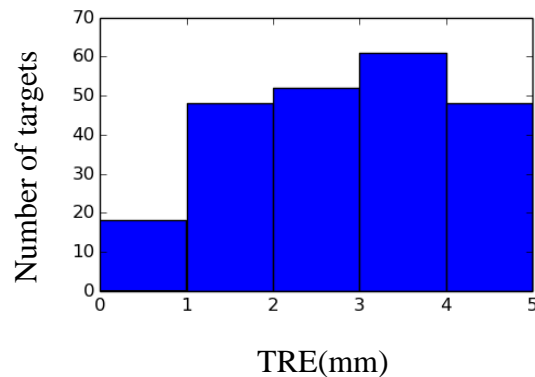


Figure 12: Histogram of TRE values associated with slice-target pairs in the subset of the targets from the BITE dataset (errors >5mm are not shown)

In summary, my approach is as follows:

- skull strip MR data and estimate segmented dural surface (done with FSL-BET's default parameters);
- search for US slices that have expert identified landmarks in them from the reconstructed US volume within 0.3mm (this reduced the number of expert landmarks available, as not all expert landmarks fell so close to an US slice); and
- for each US Slice with a landmark:
 - create a rectangular craniotomy site by projecting the head of US probe onto the dural surface;
 - search for the best US probe pose using the metric and particle swarm optimizer; and
 - calculate the error between the expert identified landmarks in the US probe slice, and the MRI volume.

These steps were conducted first on one dataset (Patient 5) in a 3DOF search-space holding constant orientation, varying patch size and downsampling ratio to determine appropriate parameters for both metrics. Then those parameters were used to evaluate the performance across all data in the BITE dataset with pre-resection US images and MRI volumes. This helped determine whether BOXLC2 is a viable metric in comparison to the more established LC2.

I then evaluated the metric's capacity to direct an optimizer to the best US probe pose constrained to realistic probe poses in 6DOF. This makes the search space 2cm x 2cm x 2cm x 90° x 90° x 360°.

I determine the trade-offs in accuracy and speed between BOXLC2 and LC2 for various patch sizes by sampling the craniotomy site in 3DOF first.

2.4 Results

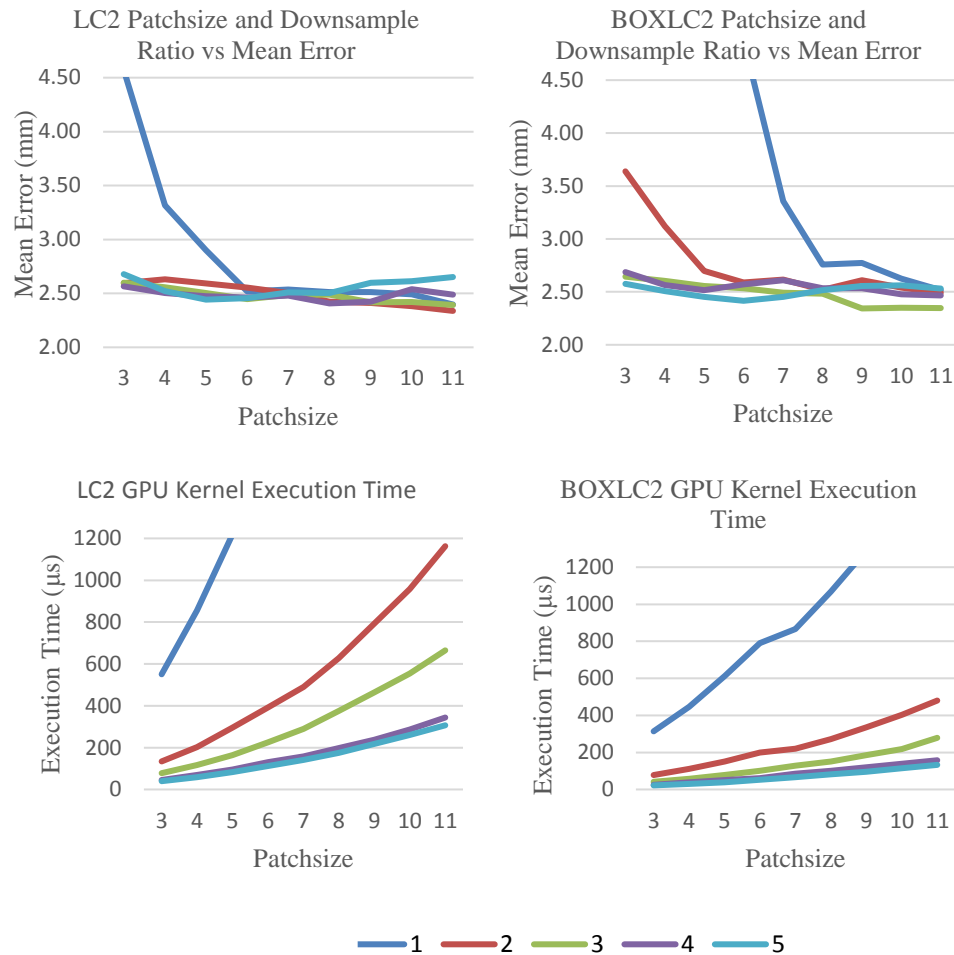


Figure 13: Comparison of BOXLC2 and LC2 with varying patch sizes and downsampling ratios resulting in different TREs and kernel execution speeds

2.4.1 3DOF Pose Recovery

Figure 13 demonstrates the effect of patch sizes between 3 and 12, as well as downsampling ratios between 1 and 5 on the TRE. Only 3DOFs were used, retaining the original orientation information from the BITE dataset. The original LC2 paper went with a 3x US downsampling ratio, to match the real-world pixel-size between MRI and US. The performance data presented in this work is generated on a PC with an Intel Core i7-4790, an Nvidia Tesla graphics processing unit, and 32GB of RAM.

As mentioned in Wein et al.⁷², there is a tradeoff between accuracy and patchsize (and thus, speed). One can see that though the metrics are similar, BOXLC2 is much more sensitive to lower patchsizes and downsample ratios. In other words, BOXLC2 requires a larger patch as measured in real-world coordinates (a function of both patchsize and downsample ratio). In this experiment, both metrics perform nearly equally well with larger downsampling ratios, with diminishing returns on larger patchsizes.

The limited data (and my desire to avoid overfitting by using more cases) prevents me from claiming these to be the most optimal parameters. This constraint also prevents me from determining BOXLC2 to be better than LC2, but I can conclude that BOXLC2 produced comparable results to the LC2 metric with a measurable improvement in speed for my implementation.

I then explored the effects BOXLC2 and LC2 using the downsampling ratios and patchsizes of 5 and 6, as well as 3 and 9, respectively. The downsampling ratio of 3, and patchsize of 9 corresponds to the experiments conducted by Wein et al.⁷² (though the aforementioned was conducted a multislice registration context).

In the original dataset, 185 slice-target pairs had a better alignment than the mean TRE of 4.1mm. After conducting the BOXLC2 registration in 3DOF with a patchsize of 6 and downsampling ratio of 5, 246 slice-target pairs had a better alignment than the original mean TRE. Similarly, the LC2 experiment running with the same parameters produced 240 slice-target pairs better than the original mean TRE.

2.4.2 6DOF Pose Recovery via Particle Swarm Optimization

Using the particle swarm optimizer described in Section 3, I searched in 6DOF for the best US pose associated with each US slice in its virtual craniotomy site (2cm x 2cm x 2cm x 90° x 90° x 360°). Table 5 presents the results. I have included some sample registrations for a visual demonstration of the algorithms successes and failures (Figure 15).

Table 4. Results from image-based registration, solving for translation components with orientation used from original dataset

| Patient No. | 1 | 2 | 3 | 4 | 5 | 6 | 7 | 8 | 9 | 10 | 11 | 12 | 13 | 14 | Mean (all slices) |
|--|-----|-----|-----|-----|-----|-----|-----|-----|-----|-----|-----|-----|-----|-----|-------------------|
| Mean Initial Error (mm) | 5.3 | 6.3 | 9.7 | 4 | 2.6 | 2.3 | 4.3 | 3.9 | 4.9 | 3 | 1.5 | 3.7 | 5 | 3.8 | 4.1 |
| BOXLC2 Mean Error (mm) Patchsize=6, Downsampling=5 | 5.4 | 2.5 | 3.4 | 2.4 | 2.4 | 3.8 | 5.1 | 3.2 | 3.6 | 2.3 | 2.8 | 3.7 | 4.1 | 3.9 | 3.4 |
| BOXLC2 Mean Error (mm) Patchsize=9, Downsampling=3 | 6.2 | 2.6 | 6 | 2.5 | 2.8 | 4.4 | 7.4 | 4.4 | 4.2 | 2.5 | 2.7 | 3.7 | 4.6 | 4.9 | 3.3 |
| LC2 Mean Error (mm) Patchsize=6, Downsampling=5 | 6.2 | 2.2 | 2.9 | 2.4 | 2.5 | 4 | 4 | 3.6 | 2.9 | 2.4 | 3.1 | 3.8 | 4.3 | 3.8 | 3.5 |
| LC2 Mean Error (mm) Patchsize=9, Downsampling=3 | 7.0 | 2.6 | 4.3 | 2.6 | 2.9 | 4.3 | 4.8 | 4.1 | 3.3 | 2.7 | 2.7 | 4 | 4.6 | 3.9 | 3.2 |

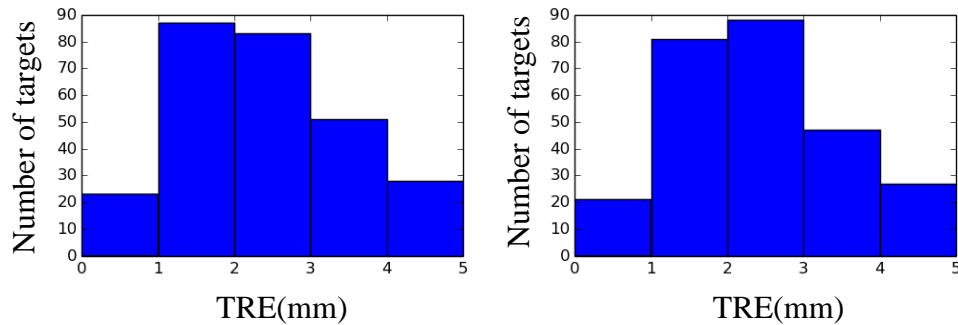


Figure 14: Histogram of TRE values for slice-target pairs in the BITE dataset from conducting a craniotomy-site constrained registration in 3DOF.

This data is also presented in histogram form in Figure 16, showing the slice-target pairs with errors less than 5mm. 135 out of the 329 slice-target pairs have a TRE less than 4.1mm (the mean initial TRE for all slices in the dataset).

6DOF Registration Visual Comparison

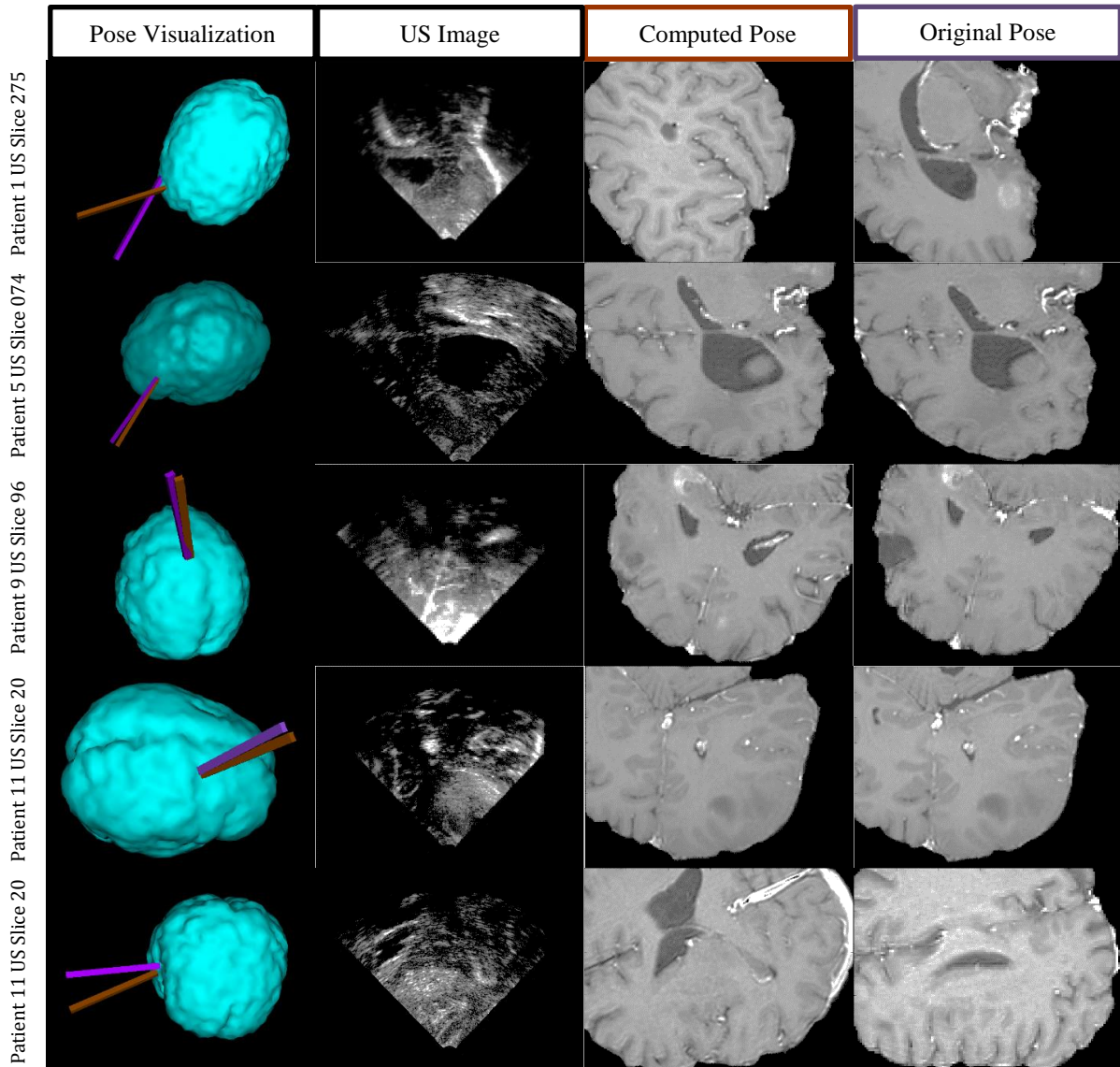


Figure 15: Some example cases from the slice based registration algorithm with calculated pose results (brown) and original pose results (purple) shown in 3D (left column) alongside the original ultrasound image (centre-left column), reformatted MRI slice corresponding to the calculated US pose (centre-right column), and reformatted MRI slice corresponding to the original US pose (right column)

Table 5: Mean TRE values associated with slice-based registration solving for the full pose of the US probe

| Patient No. | 1 | 2 | 3 | 4 | 5 | 6 | 7 | 8 | 9 | 10 | 11 | 12 | 13 | 14 |
|---|------|-------|------|-------|-------|-------|------|------|-------|------|------|------|------|------|
| Mean initial TRE | 5.3 | 6.3 | 9.7 | 4.0 | 2.6 | 2.3 | 4.3 | 3.9 | 4.9 | 3 | 1.5 | 3.7 | 5 | 3.8 |
| Mean TRE after slice-based registration | 30.7 | 10.2 | 26.7 | 9.97 | 6.82 | 18.3 | 31.3 | 19.8 | 10.5 | 12.6 | 17.5 | 16 | 17.9 | 17.6 |
| #of Poses better than the mean initial TRE for the given case | 3/32 | 18/30 | 4/13 | 16/29 | 15/28 | 14/35 | 5/15 | 5/22 | 12/19 | 5/20 | 3/24 | 8/19 | 7/21 | 7/22 |

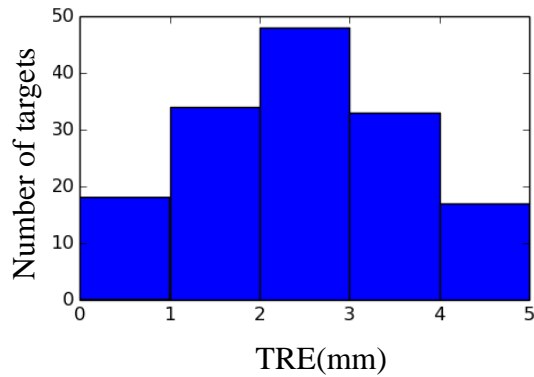


Figure 16: Histogram of TRE values for slice-target pairs with poses resulting from Particle Swarm optimization with the BOXLC2 metric (slice-target pairs with TRE values >5mm are not shown)

2.5 Discussion

I have presented BOXLC2, a variation on the LC2 metric, which produces a measurable speed improvement over LC2, while retaining similar performance in the context of 2D slice-to-volume registration. However, it is difficult to determine whether a given implementation is the most efficient for all GPU hardware. I would expect that if shared memory increases on GPUs, the cost of accessing global and shared memory in LC2 a second time would be mitigated (as several rows of pixels could be loaded into shared memory at once instead of needing to load one row at a time into shared memory twice).

My results show that for a given pose, one can recover the translation components of an US probe for a given individual US slice to a degree of accuracy comparable to or better than the mean initial errors in the BITE dataset. As the orientation components of the pose were the most problematic, one can envision a system where an inertial measurement unit and gyroscope sensor help constrain the range of possible orientations to guide the algorithm to the correct US probe pose. This embodiment could also constrain the search space of the US probe using image-based techniques such as speckle-tracking^{90,113}. Segmenting structures in US and MRI may also aid with correcting for distortions caused by a mismatch between the speed of sound for a given tissue and the speed of sound assumed by the US machine.

The 6DOF registration attempt was unsuccessful. In the dataset, there are ultrasound images that have too few or too weak features, regions that fall outside the skull-stripped brain boundary, and/or potential MRI slices that have structures that align better with the single slice's-image data. All of these factors make it challenging to register the US slices. It would be interesting to see if there is potential to develop a better measure of the structural information in an US slice beyond the patch-wise US image variance as used by Wein et al.¹⁰⁵ and then use this measure to identify slices that are more prone to positioning error per this algorithm.

With any experiment that operates on small numbers of patient cases, such as ours, there is a risk of overfitting the parameters to match the data. To avoid overfitting the limited data, I chose to develop the similarity metric using just one of the cases (Case 5). There is sufficient heterogeneity within US-probe registration and the MRI volumes in the BITE dataset to mitigate some of the risk. There is additional risk from the fact that the metric is based on another that was validated on the same BITE dataset. Consequently, I acknowledge that this data may be insufficient to arrive at a firm conclusion and look forward to experimenting with more sources of data in the future. This experiment is further limited by the fact that a given target's depth will affect the resultant TRE values.

Chapter 3

3 An Unscented Kalman Filter Multi-Data Fusion Algorithm for Neurosurgical Ultrasound Guidance

3.1 Background

As presented in Chapter 2, the 2D-3D registration shows promise in the context of localizing slices that are constrained in orientation, but free to move in translation. Consequently, a sensor that is able to constrain or partially constrain the ultrasound probe orientation may provide a feasible MRI-guided ultrasound system without some of the drawbacks of optical tracking.

As described in Section 1.8, my goal is to develop a system that is able to function in pre-resection workflow to avoid introducing complicated arrangements to maintain acoustic coupling in the resection cavity, and acoustic enhancement artefacts. In constraining the workflow for this system, I hope to make progress towards a system that

- adds minimal hardware;
- is free from calibration, or requires minimal calibration;
- is free of manual registration, or robust to large registration errors;
- is independent of ultrasound systems;
- is less sensitive to line-of-sight issues;
- can be an optional adjunct to an existing optical tracking session, providing line-of-sight correction; and
- provides brain shift visualization.

To fuse the 2D-3D Image-based registration with the sensor measurements, I employ a Kalman Filter. The essence of this powerful algorithm based on Bayes' theorem is that the model of the system, combined with a model of the various sensors that are indirectly measuring the system, can yield a more precise estimate of the state of that system.

There has been significant work in and outside of the surgical image guidance literature on the use of Kalman Filtering in its various forms. Within the medical imaging field it has been employed for registering point clouds derived from 3D ultrasound images and CT volumes^{114,115}, fusing optical and magnetic tracking systems¹⁰⁰, fusing inertial and magnetic tracking sensors¹¹⁶, and fusing electromagnetic tracking with speckle-tracked 3D freehand ultrasound⁹⁸.

3.2 Methods

3.2.1 Overview

The same PyCUDA-enabled Python module utilized in Chapter 2 was modified to include an unscented Kalman filtering and smoothing provided by the pykalman¹¹⁷ library. In addition, the module enabled virtual craniotomy sites to be defined manually in Slicer.

3.2.2 Unscented Kalman Filtering and Smoothing

The unscented Kalman filter is an extension to the Kalman filter to enable non-linear state transition equations¹¹⁸⁻¹²⁰. The unscented Kalman filter propagates a few sample points called sigma points located at the mean and symmetrically along the principle axis of the confidence ellipsoid through the non-linear system model to estimate the posterior mean and covariance. To refine prior ultrasound poses as incoming data is captured, I employ the Unscented Kalman Smoothing algorithm which refines prior poses as new poses are computed.

I am including two different system models in the evaluation. The first has 15 state variables – three translation variables with two derivatives each, and three yaw-pitch-roll Euler angle variables and their first derivatives. The second system includes the state variables of the first along with three gyroscope bias terms, and three orientation placement error terms for allowing for the calibration of the inertial unit on the on the ultrasound probe (thus, the model has 21 state variables). A drawback of this system model is the use of Euler angles, which leave the possibility open for mathematical singularities¹²¹ in the algorithm. However, in testing, issues only arose if the posterior state covariance neared π (as there would be multiple solutions to a given pose). The Euler angle simplification

allowed me to use the same state variables within the search space of the particle swarm optimizer with minimal modification

The state transition covariance was derived from an assumption that the acceleration of the probe will be discontinuous and discrete at each time step per filterpy library's `discrete_white_noise` function¹²², assuming a typical acceleration step of 60mm/s^2 and a typical angular velocity step of 2rad/s .

To fuse the 2D/3D registration algorithm described in Chapter 2, I conducted preliminary experiments using the particles from the particle-swarm to provide the measurement-update covariance. Unfortunately, this made for an unstable algorithm, occasionally shrinking the posterior covariance to a miniscule point. Consequently, I settled on using a fixed measurement-update covariance to yield consistent and reproducible results.

3.2.3 Particle Swarm Optimizer

The particle swarm optimizer is the same as in Section 2.2.4, with the exception that its constraint is formed by the union of the craniotomy site and the posterior covariance ellipsoid from the UKF. Particles that exit the constraint criteria are given an infinite cost. The number of particles also varies with the volume of the ellipsoid. I used 200 iterations with a particle count ranging from 800 to 25000 proportional to the volume of the 99.5% percentile confidence ellipsoid. These changes helped convergence within the ellipsoidal shape.

3.2.4 Simulated Data

I once again employed the Brain Images for Tumour Evaluation (BITE) Database as the source for testing data. However, as the BITE database does not include inertial measurements, I had to generate these synthetically. This was achieved by

- taking the second differences of each translational measurement in the dataset;
- smoothing each component of the differences alongside orientation components with the Lowess smoothing built into Matlab; and

- using the MATLAB Simulink “Three Axis Inertial Measurement Unit” block to transform the above second derivatives into IMU measurements (adding the effects of gravity). The noise power terms were generated from the specifications sheet of the PhidgetSpatial inertial measurement unit from Phidgets¹²³.

Craniotomy sites were manually defined for each of the patients using four points on the segmented brain surface. The software allows 1.6cm into and out of the brain to allow for brain-shift correction, if needed.

To make the simulation more realistic, the orientations for each patient were perturbed in a randomly chosen direction by five degrees, thus, giving an opportunity for the algorithm to show its ability to handle calibration/placement/registration error.

This approach has inherent limitations, as the motions recorded in the optical tracking data in the BITE data may not be representative of what happens in other operating rooms. In addition, the simulated noise may not sufficiently capture the noise dynamics of the sensor hardware.

3.2.5 Phantom Experiments

An off-the-shelf MRI PVA phantom was used for multi-modal US-MRI imaging. The phantom was submerged in a plastic container and placed on a neoprene sheet to aid with reducing reflection artefacts in the ultrasound image.

After I conducted an MRI scan of the phantom, an optically-navigated ultrasound workflow was set up using Slicer¹⁰⁶, PLUS¹²⁴, a Northern Digital Polaris Spectra optical tracking system, and an Ultrasonix L-14 probe. In addition, a PhidgetSpatial Precision 3/3/3 High Resolution inertial measurement unit was attached to the ultrasound probe, forming an inertial/optical hybrid tracking system.

Touch point registration was performed in Slicer using the six multimodal fiducial markers. Tracker to ultrasound calibration was done using the Z-Bar phantom calibration hardware and routines in the PLUS library. Data were collected with several participants

performing the experiment imaging around the locations of simulated tumours in the phantom. Virtual craniotomy sites were added after the fact.

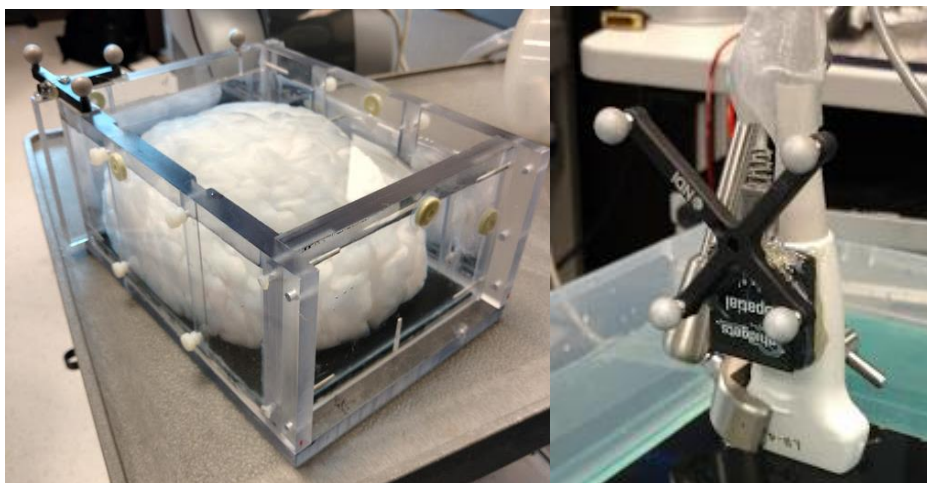


Figure 17: Multi-Modal Phantom (left) and ultrasound probe instrumented with IMU and optical tracker (Right)

3.2.6 Analysis

I present individual TRE Histograms for each case along with a cumulative TRE histogram using the same landmarks that were part of the analysis in Chapter 2. The TRE histograms give a sense of the precision and accuracy of the algorithms when looking at clinically relevant errors. Outliers, like in Chapter 2, are defined as TREs $>5\text{mm}$, and are excluded from the histograms.

3.2.7 MRI-Guided Neurosurgical Ultrasound with Image-Registration and Inertial Tracking Only

In this experiment, I assume an approximate initial orientation knowledge of the IMU and ultrasound probe with respect to the patient (within ten degrees). The translational components are initialized with the centroid of the craniotomy site. The registration “measurements” were given a covariance value of 100mm^2 in the translation components, and $0.4^{\circ 2}$ in the orientation components. The large measurement update covariance helps the algorithm recover from false positives in the similarity metric.

3.2.8 Line of Sight Correction in an MRI-Guided Ultrasound System Using Inertial Measurements and Image-Based Registration

In this experiment, I used the first frame of optical tracking data to initialize the ultrasound probe location, and allowed for the inertial measurements and 2D/3D registration to locate the ultrasound probe location. The registration “measurements” were given a covariance value of 64mm^2 in the translation components, and $0.2^{\circ 2}$ in the orientation components.

3.2.9 Analysis

As in Chapter 2, I use the expert identified landmarks in the BITE dataset to validate the algorithms as I do not have a patient dataset with ground-truth ultrasound poses.

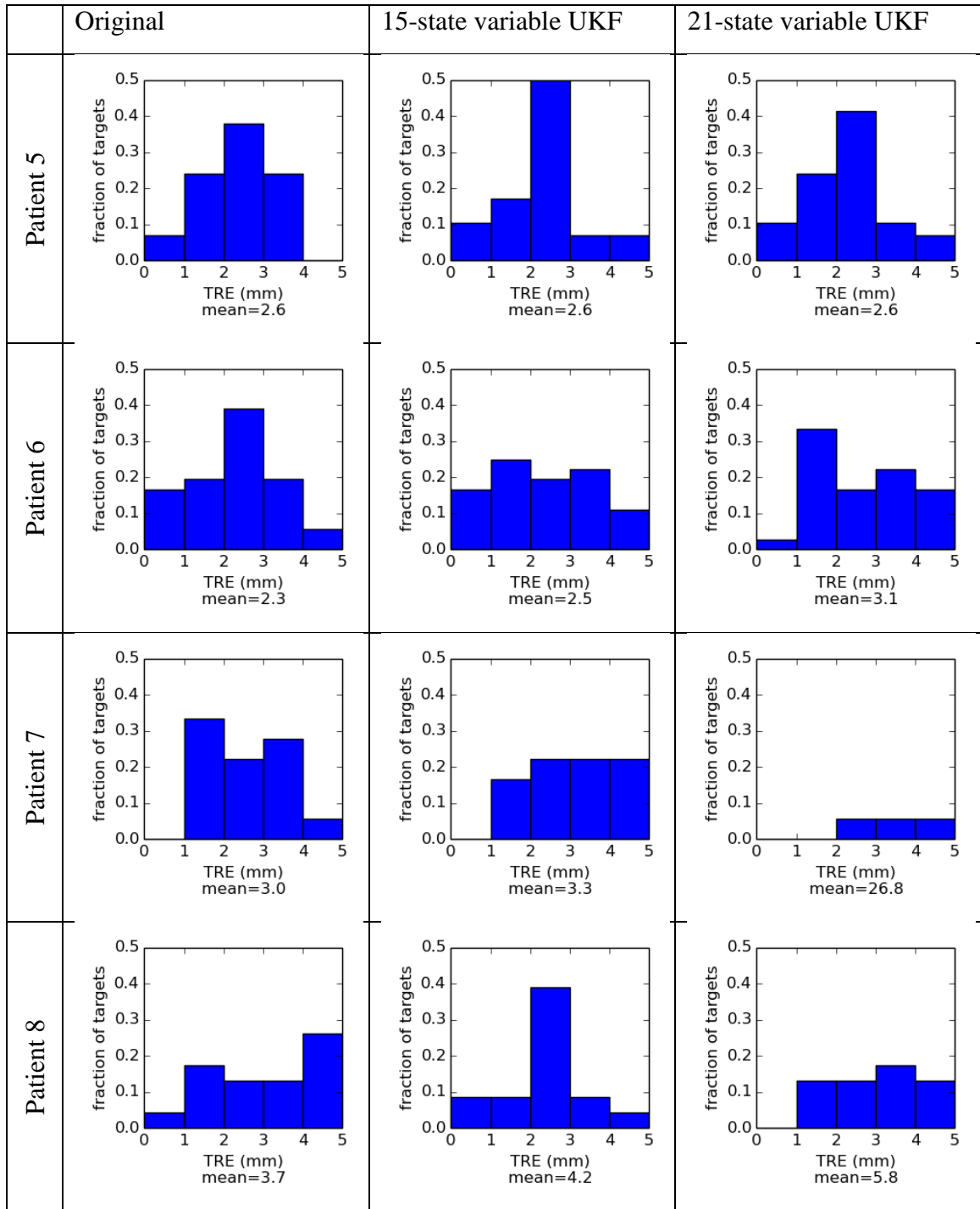
3.3 Results

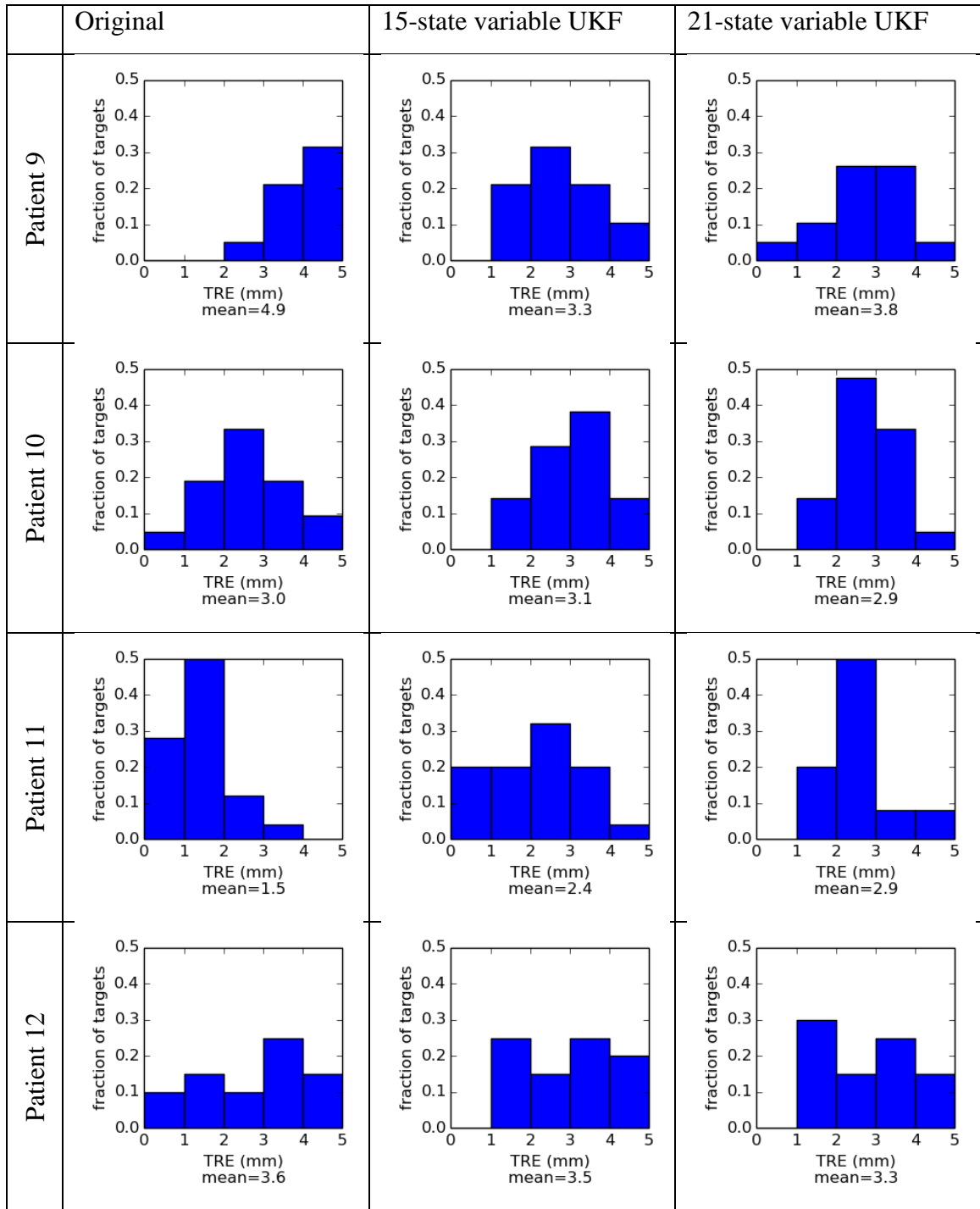
3.3.1 Line of Sight Correction Using UKF Algorithm

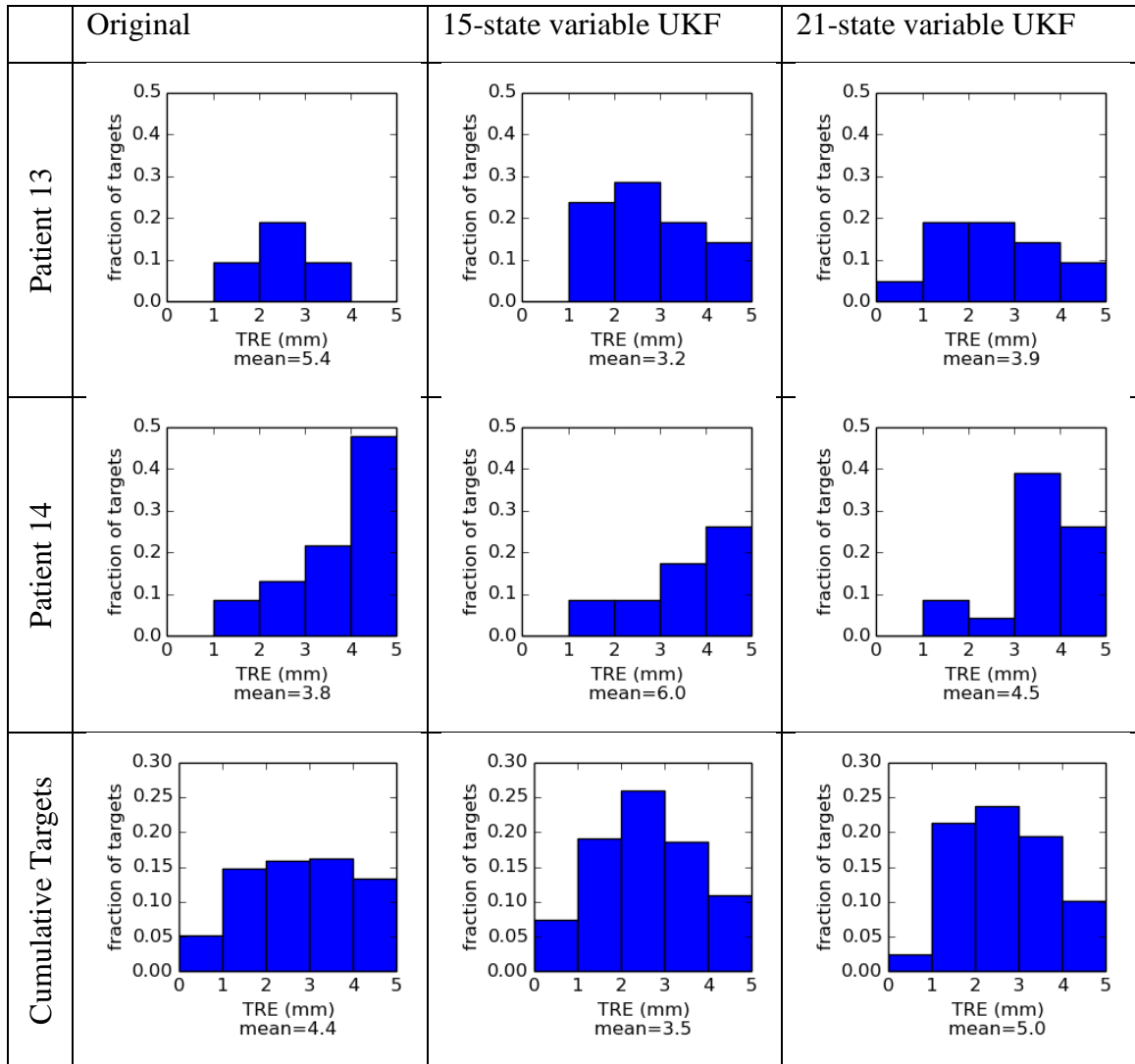
I find very comparable TRE histograms when comparing the optically tracked probe and the probe tracked with the optical/inertial/registration tracking. The UKF algorithm with additional state variables suffers a penalty with regards to accuracy. Looking at the cumulative results, the 15-state UKF algorithm has a lower mean TRE than the original data, where the 21-state algorithm does not. The histograms show that there are fewer outliers than in both versions of the UKF algorithm. The 15-state UKF algorithm produces a comparable mean TRE (within 2.5 mm or better than the optical tracking) in each case except for patient 14. The 21-state UKF algorithm produces a comparable mean TRE in 11 of 14 patient cases (Table 6) although it occasionally generated very large outliers, as shown in patient 7, since the search space was large enough that the registration algorithm could fall into a false optimum point in the similarity function far away. Both algorithms required 15 seconds per frame in my implementation running on a PC with an Intel Core i7-4790, an Nvidia Tesla graphics processing unit, and 32GB of RAM.

Table 6: Comparing TRE histograms between the UKF sensor fusion line-of-sight correction algorithms to the original data.

| | Original | 15-state variable UKF | 21-state variable UKF |
|-----------|--|--|--|
| Patient 1 | <p>fraction of targets</p> <p>TRE (mm)</p> <p>mean=5.2</p> | <p>fraction of targets</p> <p>TRE (mm)</p> <p>mean=5.5</p> | <p>fraction of targets</p> <p>TRE (mm)</p> <p>mean=9.0</p> |
| Patient 2 | <p>fraction of targets</p> <p>TRE (mm)</p> <p>mean=6.4</p> | <p>fraction of targets</p> <p>TRE (mm)</p> <p>mean=2.2</p> | <p>fraction of targets</p> <p>TRE (mm)</p> <p>mean=2.3</p> |
| Patient 3 | <p>fraction of targets</p> <p>TRE (mm)</p> <p>mean=9.3</p> | <p>fraction of targets</p> <p>TRE (mm)</p> <p>mean=5.0</p> | <p>fraction of targets</p> <p>TRE (mm)</p> <p>mean=3.7</p> |
| Patient 4 | <p>fraction of targets</p> <p>TRE (mm)</p> <p>mean=4.0</p> | <p>fraction of targets</p> <p>TRE (mm)</p> <p>mean=2.2</p> | <p>fraction of targets</p> <p>TRE (mm)</p> <p>mean=2.4</p> |





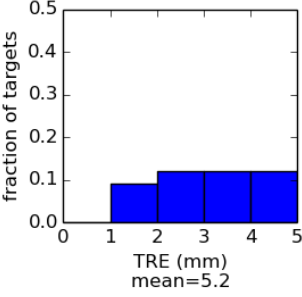
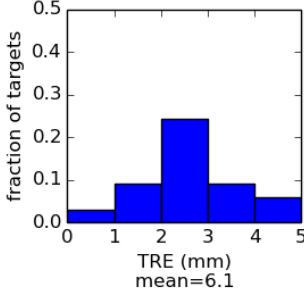
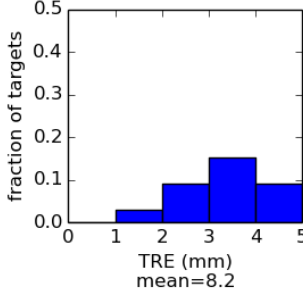
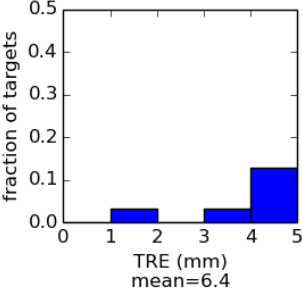
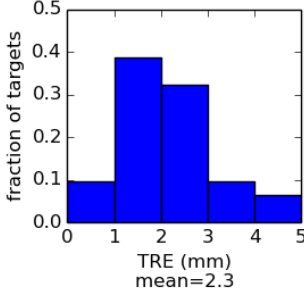
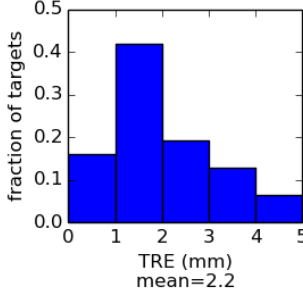
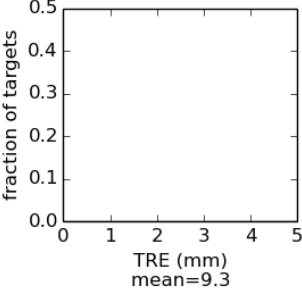
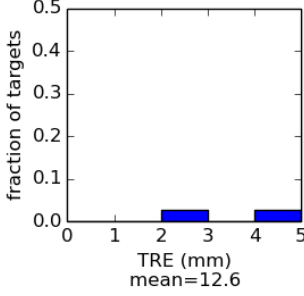
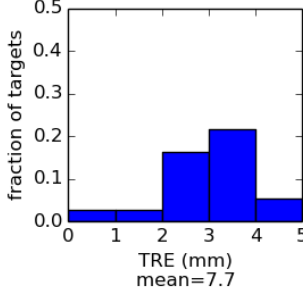


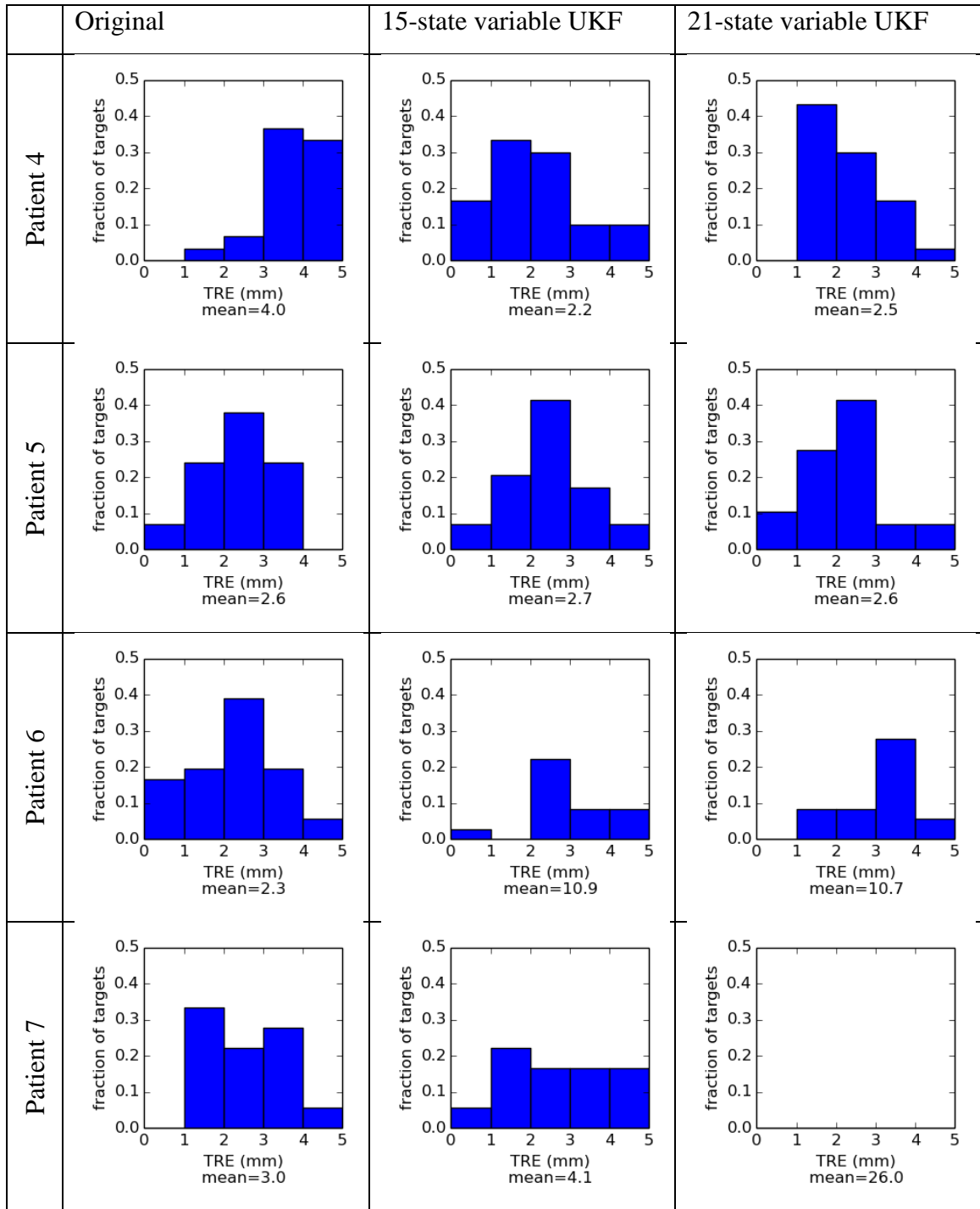
3.3.2 MRI-Guided Ultrasound Without a Conventional Tracking System

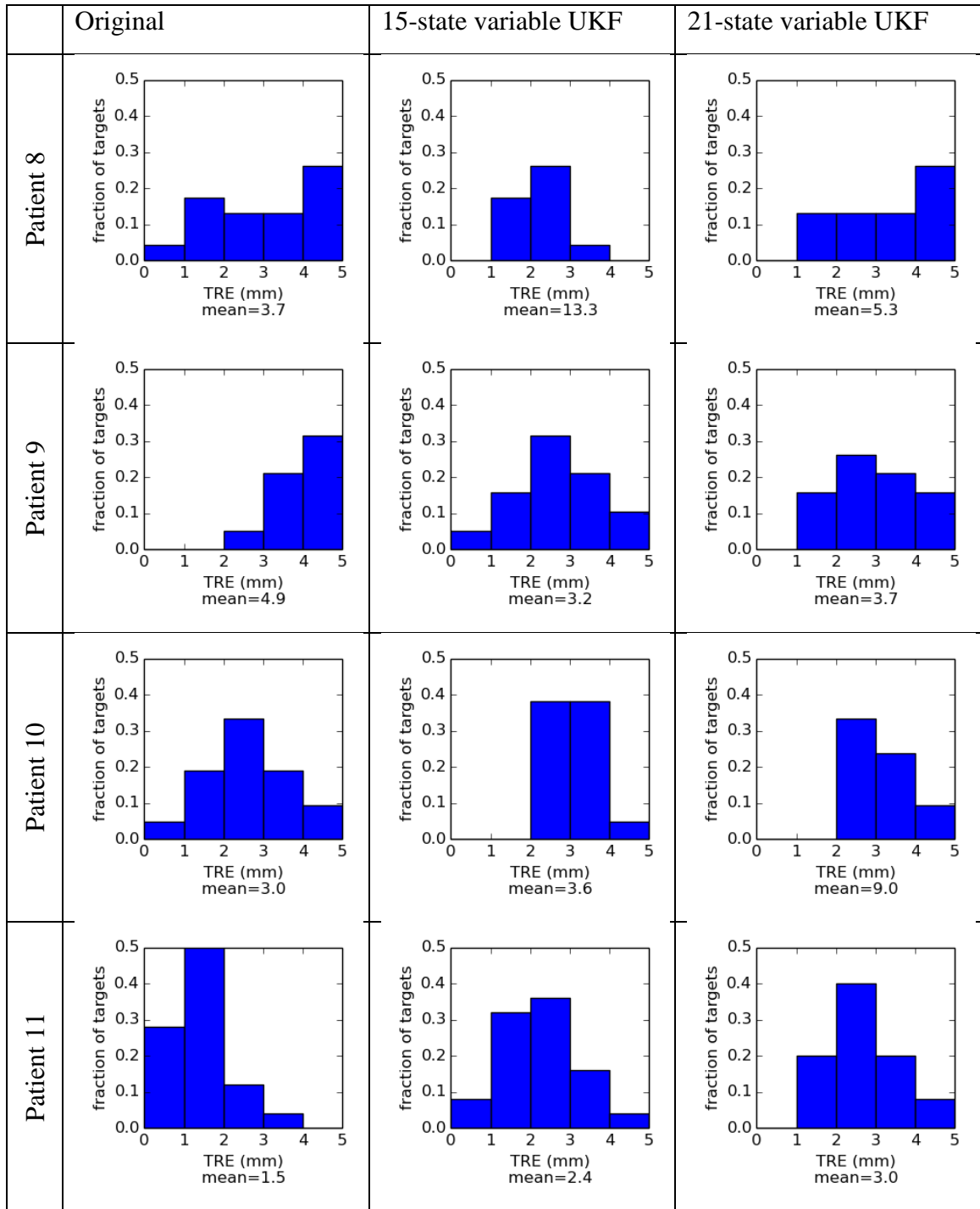
Here one finds an accuracy penalty introduced by having a less constrained initialization (Table 7). The UKF algorithm is able to recover the ultrasound poses with a comparable accuracy (within 2.5mm or better than optical) in 10 out of 14 cases using the simpler UKF algorithm with 15 state variables. Just as with the line-of-sight correction algorithm, I see an accuracy penalty with moving to the 21-state variable system, with the larger search space giving opportunity for the similarity metric to guide it to false peaks. The 21-state variable algorithm also produces comparable accuracy to the original optical

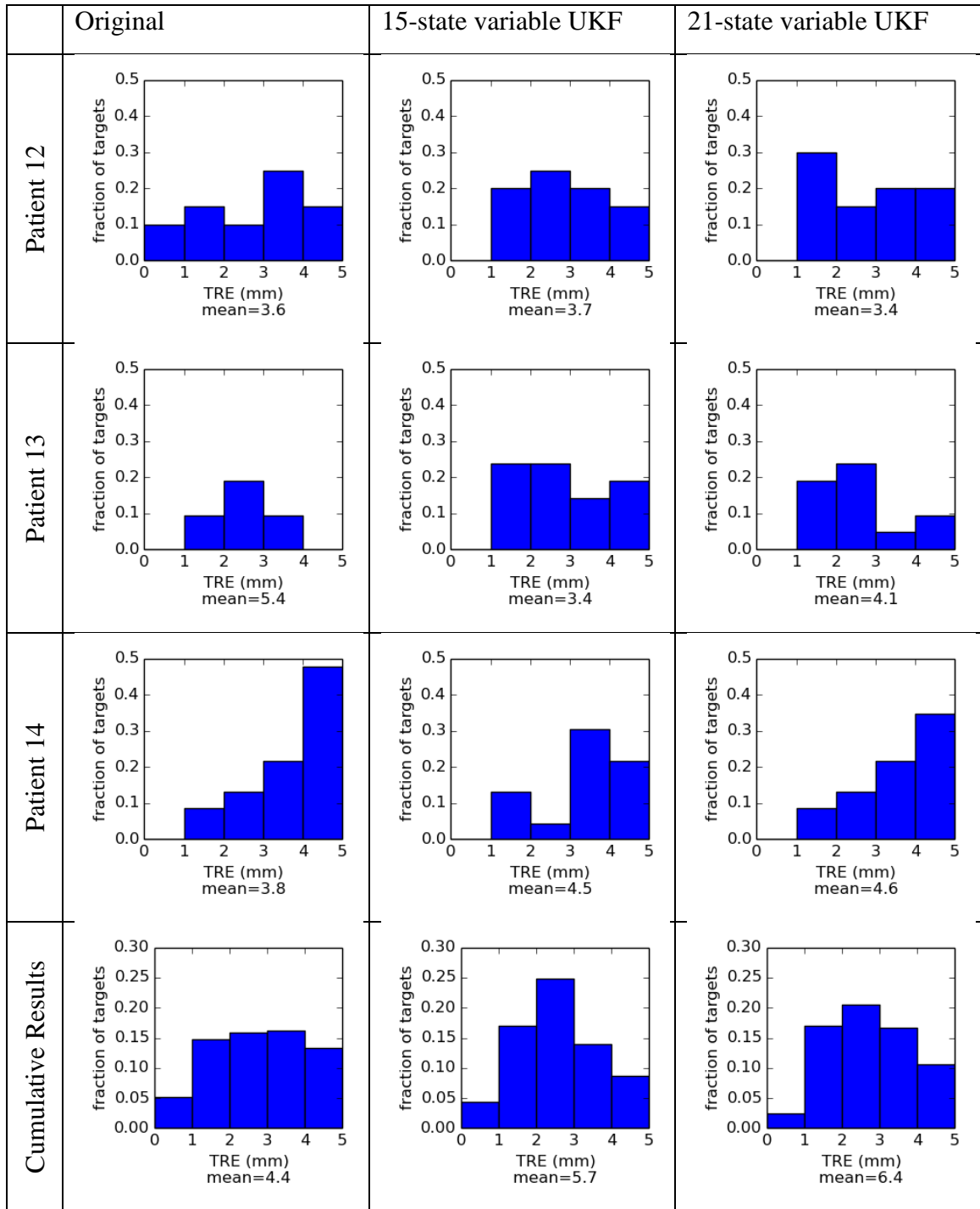
tracking data in 10 of 14 cases, but is penalized relative to the performance of the 15-state variable algorithm due to the larger search space. Both variants required approximately 370 seconds per frame at the start of ultrasound slice sequence, but settled to 15 seconds per frame as the search space of the registration shrunk with incoming data.

Table 7: Comparing TRE histograms between the UKF sensor fusion pose estimation algorithms to the original data.

| | Original | 15-state variable UKF | 21-state variable UKF |
|-----------|--|--|--|
| Patient 1 |  <p>fraction of targets</p> <p>TRE (mm)</p> <p>mean=5.2</p> |  <p>fraction of targets</p> <p>TRE (mm)</p> <p>mean=6.1</p> |  <p>fraction of targets</p> <p>TRE (mm)</p> <p>mean=8.2</p> |
| Patient 2 |  <p>fraction of targets</p> <p>TRE (mm)</p> <p>mean=6.4</p> |  <p>fraction of targets</p> <p>TRE (mm)</p> <p>mean=2.3</p> |  <p>fraction of targets</p> <p>TRE (mm)</p> <p>mean=2.2</p> |
| Patient 3 |  <p>fraction of targets</p> <p>TRE (mm)</p> <p>mean=9.3</p> |  <p>fraction of targets</p> <p>TRE (mm)</p> <p>mean=12.6</p> |  <p>fraction of targets</p> <p>TRE (mm)</p> <p>mean=7.7</p> |







3.3.3 Phantom Experiment Results

Unfortunately, the algorithm generated no meaningful data from the experiment. There are many differences between the phantom and the simulated data generated from the patient data in the BITE images. Visually, the phantom's MRI image had significant

noise on one side of the phantom. The ultrasound images had a very different visual appearance from those in the BITE dataset as well, with far fewer features contributing to the similarity metric (Figure 18 and Figure 19). The contrast to noise ratio (CNR) from MR scan of the phantom varied between 0.23 and 1.2 depending on the location in the scanning volume, where in patient one of the BITE dataset, it was 28.1. Within the ultrasound slices, the CNR was 5.8 in a representative US slice of the BITE dataset, but 0.08 from a representative slice in the phantom imaging session. CNR was calculated as the difference in mean intensity between the white/grey matter and the background divided by the variance of the background intensities in the MRI. In Ultrasound images, CNR was calculated as the difference in mean intensity between the white/grey matter and the ventricles.

I chose to use an off-the-shelf MRI brain phantom as a multi-modal imaging phantom, as it is outside the scope of this thesis to develop a high-performance multi-modality ultrasound phantom. Thus, I have noted some areas for improvement with this setup:

- the phantom was submerged under water to help with acoustic coupling, however, this reduced the apparent contrast of the cortical surface boundary;
- reflections from the bottom of the container proved to be quite hyperintense, in spite of the neoprene sheet placed underneath;
- the phantom lacked ultrasound scatterers to make a more realistic image; and
- while the phantom had ventricles, it lacked the density of structures that exist in live tissue.

I conducted a 3DOF registration experiment parallel to that conducted in 2.3. When searching a 20mm cube search space around a given ultrasound slice, I found that the similarity metric was being pulled to the extremes of the bounding box more often than not (Figure 20 and Figure 21).

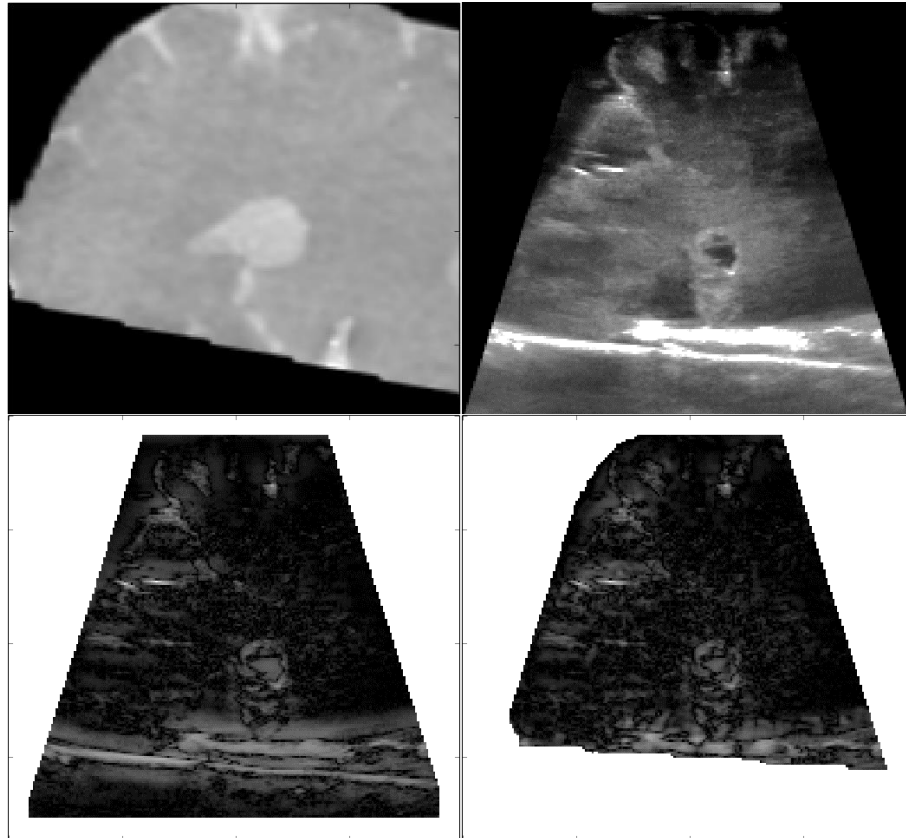


Figure 18: MR slice from original optical tracking pose (top left) alongside original ultrasound image (top right), patchwise similarity metric weight (bottom centre), and patchwise unweighted similarity (bottom left)

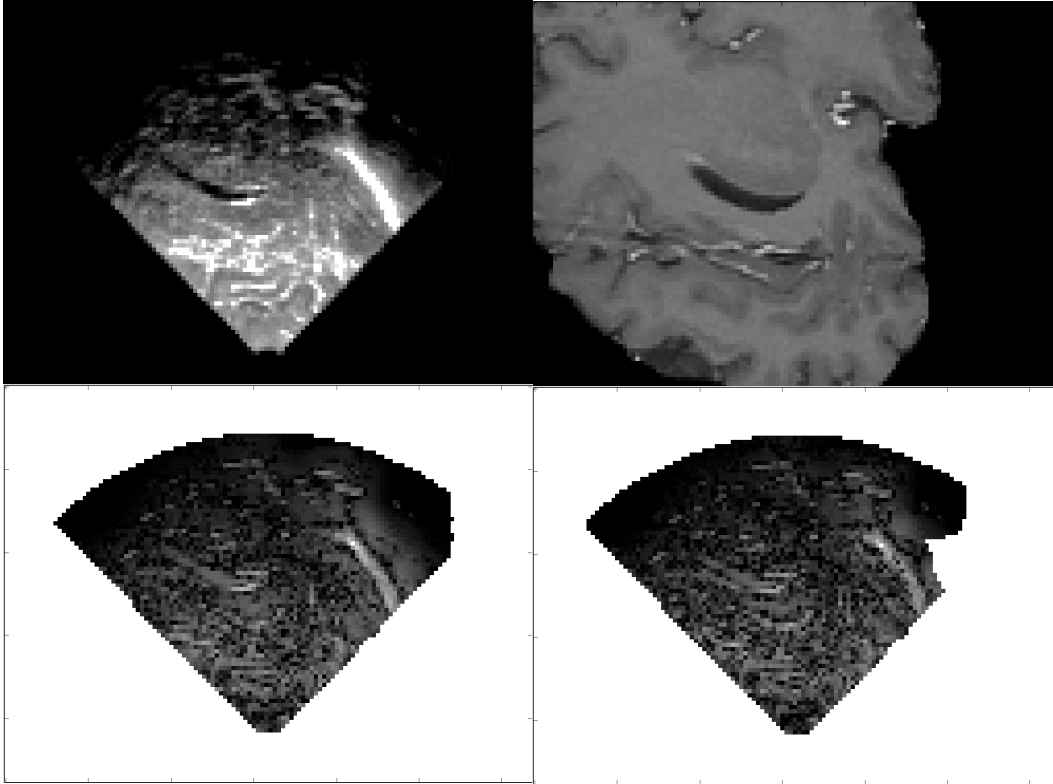


Figure 19: MR slice matching original US pose from BITE dataset (top left) alongside ultrasound image (top right), patchwise similarity metric weight (bottom centre), and patchwise unweighted similarity (bottom left)

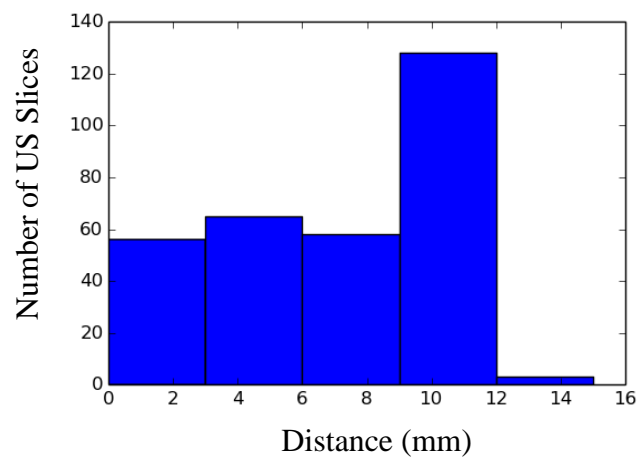


Figure 20: Histogram of distances from UKF algorithm pose to optical tracking pose

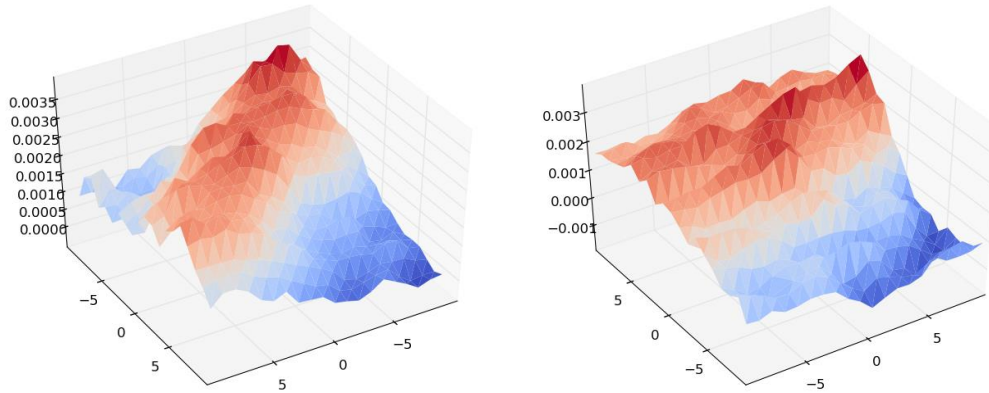


Figure 21: BOXLC2 similarity metric search space visualizations centered around the optical tracking pose in two of the failure cases showing unclear optimas in the similarity function in the translation components



5mm horizontal distortion

Figure 22: Spatial distortion in MRI image volume

The MRI volume itself had deformations of 5mm near its periphery (Figure 22) though judging by the consistently good agreement between the optically tracked

ultrasound probe and the reformatted images in Slicer, this is unlikely to be a major cause of the algorithm's registration errors (Figure 23).

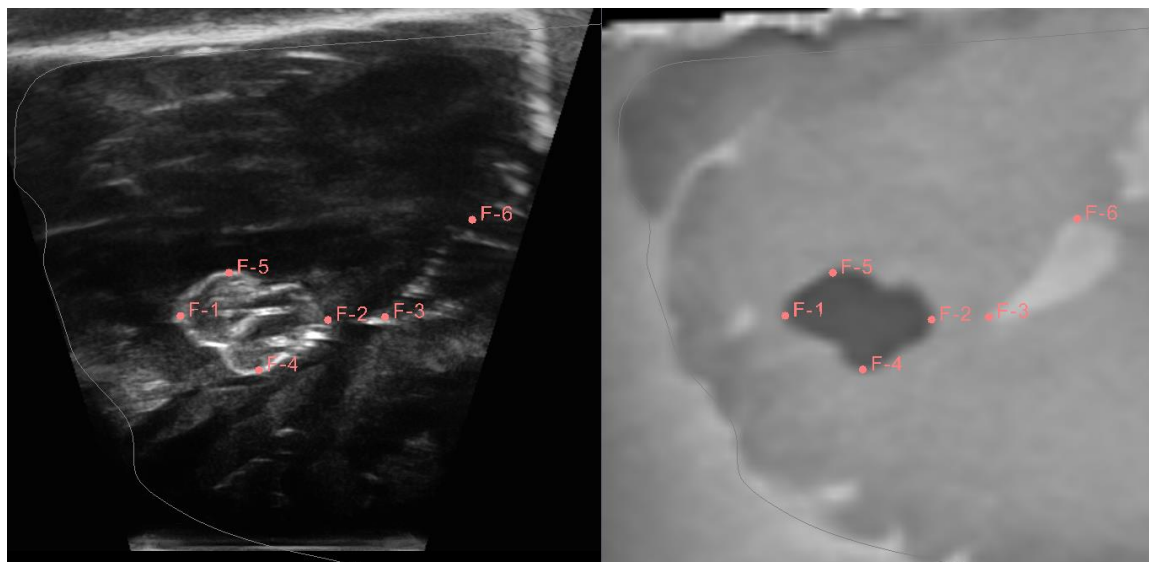


Figure 23: Example ultrasound image registered to MRI volume using optical tracking with manually placed landmarks in common co-ordinate space for visualization

I also ran the experiment without the registration-update and found that there was visually strong agreement between the orientation of the ultrasound probe generated by the UKF algorithm and the optical tracking. Thus, registration algorithm's poor performance is likely to be the source of the overall algorithm's failure.

Other strategies pursued to post-process the images included manual skull stripping, changing the gradient calculation in the similarity metric, and changing the ultrasound mask to have a shorter field of view.

3.4 Discussion

I have shown good experimental data for the UKF algorithm recovering the original pose of the ultrasound probe pose in the BITE dataset when used as a line-of-sight correction, in spite of using only one optical tracking frame as initialization. The

cumulative results indicate that there are fewer outliers with the UKF pose estimation algorithm when used in this way.

The results with the UKF algorithm running without optical tracking data are also encouraging. Both algorithms produced the comparable mean TREs in 10 out of 14 cases. The total number of outliers is also fewer for both of the UKF algorithm's results, though the results with the algorithm running as a LOS correction for optical tracking are better.

The phantom experiments may indicate a limitation with regards to drawing conclusions about the effectiveness of ultrasound-MRI multimodal similarity metrics after verification on the BITE dataset. Unfortunately, as the experiment had quite a few limitations, it is challenging to pinpoint the precise cause of the failure of the algorithm.

Neither of the algorithms presented produced real-time or near-real-time results. I revisited the line-of-sight correction experiment and ran it with 30 iterations and a maximum particle count of 1000, and found that the computation speed improved to 2 seconds per frame. The mean error of 3.5mm remained unchanged with these parameters. These faster parameters proved impractical for the UKF algorithm running without optical tracking as an initialization, with it unable to find the similarity function's optimal point.

Chapter 4

4 Conclusions

In Chapter 2, I presented a new metric based on LC2 called BOXLC2, which I developed to expedite the search for an optimal pose of a 2D US slice. I also presented the ability of the BOXLC2 similarity metric to distinguish the pose of an ultrasound probe given an MRI volume and the craniotomy site as comparable to LC2 with a measureable speed improvement. I found promise in the metric's ability to distinguish the translation components of an US pose given a small craniotomy site, though the metric was unable to recover the orientation components. To my knowledge, this is the first presentation of how a 2D/3D multimodal similarity metric functions on individual ultrasound slices in the BITE dataset.

In Chapter 3, I presented a demonstration of how a 2D/3D multi-modal similarity metric may be used in conjunction with a SLAM-like sensor/data fusion algorithm. To my knowledge, this is the first presentation of such a registration-sensor fusion algorithm in the literature. The results showed excellent results with the algorithm used as a line-of-sight corrector, augmenting the optical tracking data with synthetic inertial measurements on the BITE database. When used without the optical tracking as an initialization, the algorithm still produced meaningful TRE values. Neither algorithm operated in real-time, however with a move away from my Python implementation, it is not unrealistic to discuss the possibility for real-time performance in the future. As mentioned in 3.4, the UKF algorithm could produce reasonable accuracy as a line-of-sight corrector, operating at two seconds per frame. With smaller craniotomy sites, finer initialization from either user-input or other sensors, and faster graphics cards, I am optimistic for the evolution of this solution.

More advanced sensor fusion techniques, such as a multi-hypothesis unscented Kalman filter or particle filtering, may yield further improvements, as approximating the similarity metric's accuracy as a Gaussian of fixed variance leaves room for the algorithm to settle into false maxima, producing erroneous trajectories of the probe.

With further validation on patient data, such frameworks for ultrasound probe localization may show themselves to provide a major improvement to multi-modal ultrasound imaging sessions, providing enhanced ease of use with a minimal burden of equipment.

In this work specifically, the UKF based algorithms were able to demonstrate a potential for a system that meets the goals outlined in 3.1, though further work is necessary to validate it, as my phantom experiments were limited.

4.1 Future Work

In the short term, I expect my work will directly connect to the existing prior art in the following ways:

- the exploration of a 2D US slice to 3D MRI volume similarity metric will improve the performance of the graph-based deformable 2D-3D registration conducted by Ferrente et al.;
- estimates of the ultrasound probe location, resulting in 3D US volumes, should enable registration from the various sophisticated volumetric algorithms such as those mentioned in section 1.9.1, which would enable larger brain shift correction than that immediately provided by this algorithm; and
- the UKF algorithm should be able to incorporate existing ultrasound-based speckle correction algorithms to further enhance the pose estimation.

In the medium/long term, the work presented here can be extended in the following ways:

- gross brain shift correction may be possible by use of a monomodal US registration by combining the output of the UKF algorithm, with additional US volumes made during the procedure;
- the particles in the particle swarm optimizer for incoming frames could be initialized using the prior pose estimate, resulting in quicker convergence;
- probe calibration parameters in an optical tracking context could be solved for as state variables in the UKF algorithm;

- magnetic field biases could be solved for using the output of the registration algorithm, aiding the performance of magnetically tracked ultrasound probes in neurosurgery, as opposed to optical tracking;
- additional sensors of varying accuracy can be incorporated into the UKF algorithm; and
- image-based tracking of surgical tools within the ultrasound field of view may be possible when additional sensors are attached. For example, with an ultrasonic/time-of-flight sensor, and an IMU, the orientation and depth of a biopsy forceps can be determined. When combined with an ultrasound image of the cross-section of the forceps, all components of the biopsy forceps can be determined (Figure 24).

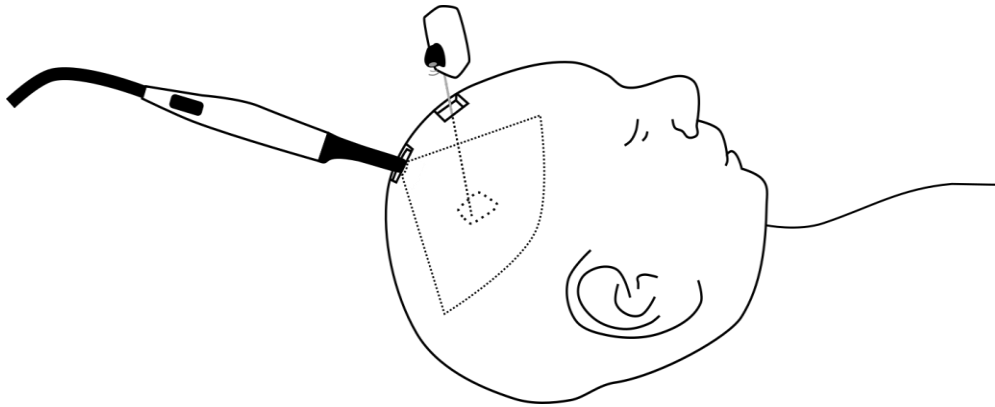


Figure 24: A multi-sensor fusion tracked biopsy forcep using image-based tracking, inertial measurements, and an ultrasonic range finder

Bibliography

- [1] Miller, D., “Intraoperative Ultrasonography in Tumor Surgery,” [Tumors of the Central Nervous System, Volume 13], M. A. Hayat, Ed., Springer Netherlands, Dordrecht, 123–135 (2014).
- [2] Tirakotai, W., Miller, D., Heinze, S., Benes, L., Bertalanffy, H., Sure, U., “A Novel Platform for Image-guided Ultrasound,” *Neurosurgery* **58**(4) (2006).
- [3] Coenen, V. A., Krings, T., Weidemann, J., Hans, F.-J., Reinacher, P., Gilsbach, J. M., Rohde, V., “Sequential Visualization of Brain and Fiber Tract Deformation during Intracranial Surgery with Three-dimensional Ultrasound: An Approach to Evaluate the Effect of Brain Shift,” *Neurosurgery*, 133–141 (2005).
- [4] Unsgaard, G., Rygh, O. M., Selbekk, T., Müller, T. B., Kolstad, F., Lindseth, F., Hernes, T. A. N., “Intra-operative 3D ultrasound in neurosurgery,” *Acta Neurochir. (Wien)* **148**(3), 235–253 (2006).
- [5] Tronnier, V. M., Bonsanto, M. M., Staubert, A., Knauth, M., Kunze, S., Wirtz, C. R., “Comparison of intraoperative MR imaging and 3D-navigated ultrasonography in the detection and resection control of lesions,” *Neurosurg. Focus* **10**(2), 1–5 (2001).
- [6] Moiyadi, A. V., Shetty, P. M., Mahajan, A., Udare, A., Sridhar, E., “Usefulness of three-dimensional navigable intraoperative ultrasound in resection of brain tumors with a special emphasis on malignant gliomas,” *Acta Neurochir. (Wien)* **155**(12), 2217–2225 (2013).
- [7] Woodworth, G. F., McGirt, M. J., Samdani, A., Garonzik, I., Olivi, A., Weingart, J. D., “Frameless image-guided stereotactic brain biopsy procedure: diagnostic yield, surgical morbidity, and comparison with the frame-based technique,” *J. Neurosurg.* **104**(2), 233–237 (2006).
- [8] Grossman, R., Sadetzki, S., Spiegelmann, R., Ram, Z., “Haemorrhagic complications and the incidence of asymptomatic bleeding associated with stereotactic brain biopsies,” *Acta Neurochir. (Wien)* **147**(6), 627–631 (2005).
- [9] Bernstein, M., Parrent, A. G., “Complications of CT-guided stereotactic biopsy of intra-axial brain lesions,” *J. Neurosurg.* **81**(2), 165–168 (1994).
- [10] Bernays, R. L., Kollias, S. S., Khan, N., Brandner, S., Meier, S., Yonekawa, Y., “Histological yield, complications, and technological considerations in 114 consecutive frameless stereotactic biopsy procedures aided by open intraoperative magnetic resonance imaging,” *J. Neurosurg.* **97**(2), 354–362 (2002).
- [11] Shetty, P., Moiyadi, A. V., “Clinical Ultrasound: Historical Aspects,” [Intraoperative Ultrasound (IOUS) in Neurosurgery], Springer, 3–8 (2016).

- [12] Ohgaki, H., “Epidemiology of Brain Tumors,” [Cancer Epidemiology], M. Verma, Ed., Humana Press, Totowa, NJ, 323–335 (2009).
- [13] Lumenta, C. B., Di Rocco, C., Haase, J., Mooij, J. J. A., eds., Neurosurgery, Springer Berlin Heidelberg, Berlin, Heidelberg (2010).
- [14] Tseng, J.-H., Merchant, E., Tseng, M.-Y., “Effects of socioeconomic and geographic variations on survival for adult glioma in England and Wales,” *Surg. Neurol.* **66**(3), 258–263 (2006).
- [15] Westphal, M., “Supratentorial Brain Tumors in Adults,” [Neurosurgery], C. B. Lumenta, C. Di Rocco, J. Haase, and J. J. A. Mooij, Eds., Springer Berlin Heidelberg, Berlin, Heidelberg, 90–96 (2010).
- [16] Prada, F., Solbiati, L., Martegani, A., DiMeco, F., B-mode, F. S., “Intraoperative Ultrasound (IOUS) in Neurosurgery.”
- [17] Kuhnt, D., Bauer, M. H., Nimsy, C., “Brain shift compensation and neurosurgical image fusion using intraoperative MRI: current status and future challenges,” *Crit. Rev. Biomed. Eng.* **40**(3) (2012).
- [18] Gobbi, D. G., Comeau, R. M., Peters, T. M., “Ultrasound Probe Tracking for Real-Time Ultrasound/MRI Overlay and Visualization of Brain Shift,” [Medical Image Computing and Computer-Assisted Intervention – MICCAI’99], C. Taylor and A. Colchester, Eds., Springer Berlin Heidelberg, Berlin, Heidelberg, 920–927 (1999).
- [19] Letteboer, M. M. J., Willems, P. W. A., Viergever, M. A., Niessen, W. J., “Brain Shift Estimation in Image-Guided Neurosurgery Using 3-D Ultrasound,” *IEEE Trans. Biomed. Eng.* **52**(2), 268–276 (2005).
- [20] Erasmus, L. J., Hurter, D., Naudé, M., Kritzing, H. G., Acho, S., “A short overview of MRI artefacts,” *SA J. Radiol.* **8**(2) (2004).
- [21] Sumanaweera., “Characterization of spatial distortion in magnetic resonance imaging and its implications for stereotactic surgery,” *Neurosurgery* **35**(4), 696 (1994).
- [22] Roberts, D. W., Hartov, A., Kennedy, F. E., Miga, M. I., Paulsen, K. D., “Intraoperative brain shift and deformation: a quantitative analysis of cortical displacement in 28 cases,” *Neurosurgery* **43**(4), 749–758 (1998).
- [23] Hartkens, T., Hill, D. L. G., Castellano-Smith, A. D., Hawkes, D. J., Maurer, C. R., Martin, A. J., Hall, W. A., Liu, H., Truwit, C. L., “Measurement and analysis of brain deformation during neurosurgery,” *IEEE Trans. Med. Imaging* **22**(1), 82–92 (2003).
- [24] Zacks, J. M., “Transformations of Visuospatial Images,” *Behav. Cogn. Neurosci. Rev.* **4**(2), 96–118 (2005).

- [25] Abhari, K., Baxter, J. S. H., Chen, E. C. S., Khan, A. R., Peters, T. M., de Ribaupierre, S., Eagleson, R., “Training for Planning Tumour Resection: Augmented Reality and Human Factors,” *IEEE Trans. Biomed. Eng.*, 1–1 (2014).
- [26] “Reprocessing Medical Devices in Health Care Settings: Validation Methods and Labeling,” Center for Biologics Evaluation and Research, US Department of Health and Human Services, FDA (2015).
- [27] Center for Devices and Radiological Health., “Guidance Documents (Medical Devices and Radiation-Emitting Products) - Guidance for Industry and FDA Staff - Information for Manufacturers Seeking Marketing Clearance of Diagnostic Ultrasound Systems and Transducers - Sections 4 Through 6 and Appendix A Through H,” <<http://www.fda.gov/MedicalDevices/DeviceRegulationandGuidance/GuidanceDocuments/ucm089001.htm>> (12 July 2016).
- [28] Widmann, G., Schullian, P., Ortler, M., Bale, R., “Frameless stereotactic targeting devices: technical features, targeting errors and clinical results: Frameless stereotactic targeting devices,” *Int. J. Med. Robot.* **8**(1), 1–16 (2012).
- [29] Dorward, N. L., Paleologos, T. S., Alberti, O., Thomas, D. G. T., “The advantages of frameless stereotactic biopsy over frame-based biopsy,” *Br. J. Neurosurg.* **16**(2), 110–118 (2002).
- [30] Smith, J. S., Quiñones-Hinojosa, A., Barbaro, N. M., McDermott, M. W., “Frame-based stereotactic biopsy remains an important diagnostic tool with distinct advantages over frameless stereotactic biopsy,” *J. Neurooncol.* **73**(2), 173–179 (2005).
- [31] Gumprecht, H. K., Darius C., W., Christianto B., L., “BrainLab VectorVision Neuronavigation System: Technology and Clinical Experiences in 131 Cases.,” *Neurosurgery* **44**(1), 97–1004 (1999).
- [32] “Medtronic StealthViz.”, <<http://www.medtronic.com/for-healthcare-professionals/products-therapies/spinal/surgical-navigation-imaging/surgical-navigation-systems/systems-software-instruments/#tab5>> (2 April 2015).
- [33] “BrightMatter™ Guide — Synaptive Medical.”, <<http://www.synaptivemedical.com/guide/>> (2 April 2015).
- [34] Verploegh, I. S. C., Volovici, V., Haitsma, I. K., Schouten, J. W., Dirven, C. M., Kros, J. M., Dammers, R., “Contemporary frameless intracranial biopsy techniques: Might variation in safety and efficacy be expected?,” *Acta Neurochir. (Wien)* **157**(11), 2011–2016 (2015).
- [35] West, J. B., Maurer, C. R., “Designing Optically Tracked Instruments for Image-Guided Surgery,” *IEEE Trans. Med. Imaging* **23**(5), 533–545 (2004).

- [36] Fitzpatrick, J. M., West, J. B., Maurer, C. R., “Predicting error in rigid-body point-based registration,” *IEEE Trans. Med. Imaging* **17**(5), 694–702 (1998).
- [37] Wiles, A. D., Thompson, D. G., Frantz, D. D., “Accuracy assessment and interpretation for optical tracking systems,” 5 May 2004, 421.
- [38] Elfring, R., de la Fuente, M., Radermacher, K., “Assessment of optical localizer accuracy for computer aided surgery systems,” *Comput. Aided Surg.* **15**(1–3), 1–12 (2010).
- [39] “IEC 60601-1:2015 - Medical electrical equipment.”, International Electrotechnical Commission.
- [40] “ISO 10993-1:2009 - Biological evaluation of medical devices -- Part 1: Evaluation and testing within a risk management process.”, Int. Stand. Organ.
- [41] Mislow, J. M. K., Golby, A. J., Black, P. M., “Origins of Intraoperative MRI,” *Neurosurg. Clin. N. Am.* **20**(2), 137–146 (2009).
- [42] Haydon, D. H., Chicoine, M. R., Dacey Jr, R. G., “The impact of high-field-strength intraoperative magnetic resonance imaging on brain tumor management,” *Neurosurgery* **60**, 92–97 (2013).
- [43] El Beltagy, M. A., Atteya, M. M. E., “The benefits of navigated intraoperative ultrasonography during resection of fourth ventricular tumors in children,” *CHILDS Nerv. Syst.* **29**(7), 1079–1088 (2013).
- [44] Unsgaard, G., Selbekk, T., Brostrup Müller, T., Ommedal, S., Torp, S. H., Myhr, G., Bang, J., Nagelhus Hernes, T. A., “Ability of navigated 3D ultrasound to delineate gliomas and metastases – comparison of image interpretations with histopathology,” *Acta Neurochir. (Wien)* **147**(12), 1259–1269 (2005).
- [45] Sæther, C., Torsteinsen, M., Torp, S., Sundstrøm, S., Unsgård, G., Solheim, O., “Did Survival Improve after the Implementation of Intraoperative Neuronavigation and 3D Ultrasound in Glioblastoma Surgery? A Retrospective Analysis of 192 Primary Operations,” *J. Neurol. Surg. Part Cent. Eur. Neurosurg.* **73**(2), 073–078 (2012).
- [46] Samii, A., Akbarian, A., Stieglitz, L., “Reliability of intraoperative high-resolution 2D ultrasound as an alternative to high-field strength MR imaging for tumor resection control: a prospective comparative study.” (2009).
- [47] Coburger, J., Scheuerle, A., Thal, D. R., Engelke, J., Hlavac, M., Wirtz, C. R., König, R., “Linear array ultrasound in low-grade glioma surgery: histology-based assessment of accuracy in comparison to conventional intraoperative ultrasound and intraoperative MRI,” *Acta Neurochir. (Wien)* **157**(2), 195–206 (2015).

- [48] Unsgaard, G., “Ultrasound-Guided Neurosurgery,” [Practical Handbook of Neurosurgery], Springer, 907–926 (2009).
- [49] Selbekk, T., Jakola, A. S., Solheim, O., Johansen, T. F., Lindseth, F., Reinertsen, I., Unsgård, G., “Ultrasound imaging in neurosurgery: approaches to minimize surgically induced image artefacts for improved resection control,” *Acta Neurochir. (Wien)* **155**(6), 973–980 (2013).
- [50] Unsgaard, G., Gronningsaeter, A., Ommedal, S., Hernes, T. A. N., “Brain operations guided by real-time two-dimensional ultrasound: new possibilities as a result of improved image quality,” *Neurosurgery* **51**(2), 402–412 (2002).
- [51] Unsgaard, G., Ommedal, S., Muller, T., Gronningsaeter, A., Hernes, T. A. N., “Neuronavigation by intraoperative three-dimensional ultrasound: initial experience during brain tumor resection,” *Neurosurgery* **50**(4), 804–812 (2002).
- [52] Prada, F., Del Bene, M., Moiraghi, A., DiMeco, F., “Echographic Brain Semeiology and Topographic Anatomy According to Surgical Approaches,” [Intraoperative Ultrasound (IOUS) in Neurosurgery], 29–39.
- [53] Hayhurst, C., Byrne, P., Eldridge, P. R., Mallucci, C. L., “Application of electromagnetic technology to neuronavigation: a revolution in image-guided neurosurgery: Technical note,” *J. Neurosurg.* **111**(6), 1179–1184 (2009).
- [54] Orringer, D. A., Golby, A., Jolesz, F., “Neuronavigation in the surgical management of brain tumors: current and future trends,” *Expert Rev. Med. Devices* **9**(5), 491–500 (2012).
- [55] Faraz, A., “In-situ Ultrasound Calibration” (2016).
- [56] Mercier, L., Del Maestro, R. F., Petrecca, K., Araujo, D., Haegelen, C., Collins, D. L., “Online database of clinical MR and ultrasound images of brain tumors,” *Med. Phys.* **39**(6), 3253–3261 (2012).
- [57] Roll, S. C., Selhorst, L., Evans, K. D., “Contribution of positioning to work-related musculoskeletal discomfort in diagnostic medical sonographers,” *Work* **47**(2), 253–260 (2014).
- [58] Evans, K., Roll, S., Baker, J., “Work-Related Musculoskeletal Disorders (WRMSD) Among Registered Diagnostic Medical Sonographers and Vascular Technologists: A Representative Sample,” *J. Diagn. Med. Sonogr.* **25**(6), 287–299 (2009).
- [59] Galloway Jr, R. L., Maciunas, R. J., Bass, W. A., Carpini, W., “Optical localization for interactive, image-guided neurosurgery,” *Med. Imaging 1994*, 137–145, International Society for Optics and Photonics (1994).

- [60] Šteňo, A., Giussani, C., Riva, M., “Multimodal Imaging in Glioma Surgery,” [Intraoperative Ultrasound (IOUS) in Neurosurgery: From Standard B-mode to Elastasonography], F. Prada, L. Solbiati, A. Martegani, and F. DiMeco, Eds., Springer International Publishing, Cham, 81–97 (2016).
- [61] Berg, D., Becker, G., “Perspectives of B-Mode Transcranial Ultrasound,” *NeuroImage* **15**(3), 463–473 (2002).
- [62] Becker, G., Berg, D., “Neuroimaging in basal ganglia disorders: perspectives for transcranial ultrasound,” *Mov. Disord.* **16**(1), 23–32 (2001).
- [63] White, P. J., Whalen, S., Tang, S. C., Clement, G. T., Jolesz, F., Golby, A. J., “An Intraoperative Brain Shift Monitor Using Shear Mode Transcranial Ultrasound Preliminary Results,” *J. Ultrasound Med.* **28**(2), 191–203 (2009).
- [64] Coburger, J., König, R. W., “Intraoperative Findings in Brain Tumor Surgery,” [Intraoperative Ultrasound (IOUS) in Neurosurgery], 41–58.
- [65] Gerganov, V. M., Samii, A., Giordano, M., Samii, M., Fahlbusch, R., “Two-dimensional high-end ultrasound imaging compared to intraoperative MRI during resection of low-grade gliomas,” *J. Clin. Neurosci.* **18**(5), 669–673 (2011).
- [66] Wells, W. M., Viola, P., Atsumi, H., Nakajima, S., Kikinis, R., “Multi-modal Volume Registration by maximization of mutual information.pdf,” *Med. Image Anal.* **1**(1), 35–51.
- [67] Roche, A., Malandain, G., Pennec, X., Ayache, N., “The correlation ratio as a new similarity measure for multimodal image registration,” [Medical Image Computing and Computer-Assisted Intervention — MICCAI’98], W. M. Wells, A. Colchester, and S. Delp, Eds., Springer Berlin Heidelberg, Berlin, Heidelberg, 1115–1124 (1998).
- [68] Roche, A., Pennec, X., Malandain, G., Ayache, N., “Rigid registration of 3-D ultrasound with MR images: a new approach combining intensity and gradient information,” *Med. Imaging IEEE Trans. On* **20**(10), 1038–1049 (2001).
- [69] Heinrich, M. P., Jenkinson, M., Bhushan, M., Martin, T., Gleeson, F. V., Brady, S. M., Schnabel, J. A., “MIND: Modality independent neighbourhood descriptor for multi-modal deformable registration,” *Med. Image Anal.* **16**(7), 1423–1435 (2012).
- [70] Sun, Y., Yuan, J., Rajchl, M., Qiu, W., Romagnoli, C., Fenster, A., “Efficient convex optimization approach to 3D non-rigid MR-TRUS registration,” [Medical Image Computing and Computer-Assisted Intervention–MICCAI 2013], Springer, 195–202 (2013).
- [71] Comeau, R. M., Sadikot, A. F., Fenster, A., Peters, T. M., “Intraoperative ultrasound for guidance and tissue shift correction in image-guided neurosurgery,” *Med. Phys.* **27**(4), 787–800 (2000).

- [72] Wein, W., Ladikos, A., Fuerst, B., Shah, A., Sharma, K., Navab, N., “Global registration of ultrasound to mri using the LC2 metric for enabling neurosurgical guidance,” [Medical Image Computing and Computer-Assisted Intervention–MICCAI 2013], Springer, 34–41 (2013).
- [73] Fuerst, B., Wein, W., Müller, M., Navab, N., “Automatic ultrasound–MRI registration for neurosurgery using the 2D and 3D LC2 Metric,” *Med. Image Anal.* **18**(8), 1312–1319 (2014).
- [74] De Nigris, D., Collins, D. L., Arbel, T., “Fast and robust registration based on gradient orientations: case study matching intra-operative ultrasound to pre-operative mri in neurosurgery,” [Information Processing in Computer-Assisted Interventions], Springer, 125–134 (2012).
- [75] Rivaz, H., Karimaghloo, Z., Fonov, V. S., Collins, D. L., “Nonrigid Registration of Ultrasound and MRI Using Contextual Conditioned Mutual Information,” *IEEE Trans. Med. Imaging* **33**(3), 708–725 (2014).
- [76] Rivaz, H., Karimaghloo, Z., Collins, D. L., “Self-similarity weighted mutual information: A new nonrigid image registration metric,” *Med. Image Anal.* **18**(2), 343–358 (2014).
- [77] Rivaz, H., Collins, D. L., “Near Real-Time Robust Non-rigid Registration of Volumetric Ultrasound Images for Neurosurgery,” *Ultrasound Med. Biol.* **41**(2), 574–587 (2015).
- [78] Jiang, D., Shi, Y., Yao, D., Wang, M., Song, Z., “miLBP: a robust and fast modality-independent 3D LBP for multimodal deformable registration,” *Int. J. Comput. Assist. Radiol. Surg.* **11**(6), 997–1005 (2016).
- [79] Kuklisova-Murgasova, M., Cifor, A., Napolitano, R., Papageorghiou, A., Quaghebeur, G., Noble, J. A., Schnabel, J. A., “Registration of 3D fetal brain US and MRI,” *Int. Conf. Med. Image Comput. Comput.-Assist. Interv.*, 667–674, Springer (2012).
- [80] Arbel, T., Arbel, T., Morandi, X., Comeau, R. M., Collins, D. L., “Automatic non-linear MRI-ultrasound registration for the correction of intra-operative brain deformations,” *Comput. Aided Surg.* **9**(4), 123–136 (2004).
- [81] Nigris, D. D., Collins, D. L., Arbel, T., “Fast rigid registration of pre-operative magnetic resonance images to intra-operative ultrasound for neurosurgery based on high confidence gradient orientations,” *Int. J. Comput. Assist. Radiol. Surg.* **8**(4), 649–661 (2013).
- [82] De Nigris, D., Mercier, L., Del Maestro, R., Collins, D. L., Arbel, T., “Hierarchical multimodal image registration based on adaptive local mutual information,” [Medical Image Computing and Computer-Assisted Intervention–MICCAI 2010], Springer, 643–651 (2010).

- [83] Ferrante, E., Paragios, N., “Graph Based Slice-to-Volume Deformable Registration,” INRIA Saclay; Center for Visual Computing, CentraleSupélec, Inria, Université Paris-Saclay (2015).
- [84] Ferrante, E., Fecamp, V., Paragios, N., “Slice-to-volume deformable registration: efficient one-shot consensus between plane selection and in-plane deformation,” *Int. J. Comput. Assist. Radiol. Surg.* **10**(6), 791–800 (2015).
- [85] De Silva, T., Fenster, A., Cool, D. W., Gardi, L., Romagnoli, C., Samarabandu, J., Ward, A. D., “2D-3D rigid registration to compensate for prostate motion during 3D TRUS-guided biopsy,” *Med. Phys.* **40**(2) (2013).
- [86] De Silva, T., Cool, D. W., Yuan, J., Romagnoli, C., Fenster, A., Ward, A. D., “Improving 2D-3D Registration Optimization Using Learned Prostate Motion Data,” [Medical Image Computing and Computer-Assisted Intervention–MICCAI 2013], Springer, 124–131 (2013).
- [87] Baumann, M., Mozer, P., Daanen, V., Troccaz, J., “Towards 3D ultrasound image based soft tissue tracking: a transrectal ultrasound prostate image alignment system,” *Int. Conf. Med. Image Comput. Comput.-Assist. Interv.*, 26–33, Springer (2007).
- [88] “UROSTATION TOUCH® – KOELIS.”, .
- [89] Dickinson, R., Hill, C., “Measurement of soft tissue motion using correlation between A-scans,” *Ultrasound Med. Biol.* **8**(3), 263–271 (1982).
- [90] Chen, J.-F., Fowlkes, J. B., Carson, P. L., Rubin, J. M., “Determination of scan-plane motion using speckle decorrelation: theoretical considerations and initial test” (1997).
- [91] Li, M., “System and method for 3-D medical imaging using 2-D scan data,” *Acoust. Soc. Am. J.* **102**, 26 (1997).
- [92] Afsham, N., Najafi, M., Abolmaesumi, P., Rohling, R., “Out-of-plane motion estimation based on a Rician-Inverse Gaussian model of RF ultrasound signals: speckle tracking without fully developed speckle,” 23 February 2012, 832017.
- [93] Afsham, N., Najafi, M., Abolmaesumi, P., Rohling, R., “A Generalized Correlation-Based Model for Out-of-Plane Motion Estimation in Freehand Ultrasound,” *IEEE Trans. Med. Imaging* **33**(1), 186–199 (2014).
- [94] Narges, A., “Speckle tracking for 3D freehand ultrasound reconstruction,” University of British Columbia (2014).
- [95] Schretter, C., Sun, J., Bundervoet, S., Dooms, A., Schelkens, P., de Brito Carvalho, C., Slagmolen, P., D’hooge, J., “Continuous Ultrasound Speckle Tracking with Gaussian Mixtures,” *Eng. Med. Biol. Conf.* (2015).

- [96] Krupa, A., Fichtinger, G., Hager, G. D., “Real-time Motion Stabilization with B-mode Ultrasound Using Image Speckle Information and Visual Servoing,” *Int. J. Robot. Res.* **28**(10), 1334–1354 (2009).
- [97] Mebarki, R., Krupa, A., Chaumette, F., “2-d ultrasound probe complete guidance by visual servoing using image moments,” *Robot. IEEE Trans. On* **26**(2), 296–306 (2010).
- [98] Lang, A., Mousavi, P., Fichtinger, G., Abolmaesumi, P., “Fusion of electromagnetic tracking with speckle-tracked 3D freehand ultrasound using an unscented Kalman filter,” 26 February 2009, 72651A.
- [99] Goldsmith, A. M., Pedersen, P. C., Szabo, T. L., “An inertial-optical tracking system for portable, quantitative, 3D ultrasound,” presented at Ultrasonics Symposium, November 2008, 45–49, IEEE.
- [100] Vaccarella, A., De Momi, E., Enquobahrie, A., Ferrigno, G., “Unscented Kalman Filter Based Sensor Fusion for Robust Optical and Electromagnetic Tracking in Surgical Navigation,” *IEEE Trans. Instrum. Meas.* **62**(7), 2067–2081 (2013).
- [101] Lang, A., Mousavi, P., Gill, S., Fichtinger, G., Abolmaesumi, P., “Multi-modal registration of speckle-tracked freehand 3D ultrasound to CT in the lumbar spine,” *Med. Image Anal.* **16**(3), 675–686 (2012).
- [102] Thrun, S., Burgard, W., Fox, D., *Probabilistic robotics*, MIT press (2005).
- [103] Yavariabdi, A., Bartoli, A., Samir, C., Artigues, M., Canis, M., “Mapping and characterizing endometrial implants by registering 2D transvaginal ultrasound to 3D pelvic magnetic resonance images,” *Comput. Med. Imaging Graph.* **45**, 11–25 (2015).
- [104] Xishi Huang., Moore, J., Guiraudon, G., Jones, D. L., Bainbridge, D., Jing Ren., Peters, T. M., “Dynamic 2D Ultrasound and 3D CT Image Registration of the Beating Heart,” *IEEE Trans. Med. Imaging* **28**(8), 1179–1189 (2009).
- [105] Wein, W., Brunke, S., Khamene, A., Callstrom, M. R., Navab, N., “Automatic CT-ultrasound registration for diagnostic imaging and image-guided intervention,” *Med. Image Anal.* **12**(5), 577–585 (2008).
- [106] Fedorov, A., Beichel, R., Kalpathy-Cramer, J., Finet, J., Fillion-Robin, J.-C., Pujol, S., Bauer, C., Jennings, D., Fennessy, F., et al., “3D Slicer as an Image Computing Platform for the Quantitative Imaging Network,” *Magn. Reson. Imaging* **30**(9), 1323–41 (2012).
- [107] Fuerst, B., “LC2Code,” LC2Code, <<http://campar.in.tum.de/Main/LC2Code>> (12 August 2015).

- [108] Jähne, B., Scharr, H., Körkel, S., “Principles of filter design,” *Handb. Comput. Vis. Appl.* **2**, 125–151 (1999).
- [109] Eberhart, R. C., Kennedy, J., “A new optimizer using particle swarm theory,” *Proc. Sixth Int. Symp. Micro Mach. Hum. Sci.* **1**, 39–43, New York, NY (1995).
- [110] Shi, Y., “Particle swarm optimization: developments, applications and resources,” presented at evolutionary computation, 2001. *Proceedings of the 2001 Congress on, 2001*, 81–86, IEEE.
- [111] “tisimst/pyswarm.”, GitHub, <<https://github.com/tisimst/pyswarm>> (8 August 2016).
- [112] Jenkinson, M., Beckmann, C. F., Behrens, T. E., Woolrich, M. W., Smith, S. M., “Fsl,” *Neuroimage* **62**(2), 782–790 (2012).
- [113] Tuthill, T. A., Krücker, J. F., Fowlkes, J. B., Carson, P. L., “Automated three-dimensional US frame positioning computed from elevational speckle decorrelation,” *Radiology* **209**(2), 575–582 (1998).
- [114] Moghari, M. H., Abolmaesumi, P., “A novel incremental technique for ultrasound to CT bone surface registration using unscented Kalman filtering,” *Int. Conf. Med. Image Comput. Comput.-Assist. Interv.*, 197–204, Springer (2005).
- [115] Moghari, M. H., Abolmaesumi, P., “Point-Based Rigid-Body Registration Using an Unscented Kalman Filter,” *IEEE Trans. Med. Imaging* **26**(12), 1708–1728 (2007).
- [116] Hongliang Ren., Rank, D., Merdes, M., Stallkamp, J., Kazanzides, P., “Multisensor Data Fusion in an Integrated Tracking System for Endoscopic Surgery,” *IEEE Trans. Inf. Technol. Biomed.* **16**(1), 106–111 (2012).
- [117] “pykalman — pykalman 0.9.2 documentation.”, <<http://pykalman.github.io/>> (18 July 2016).
- [118] Julier, S. J., Uhlmann, J. K., “New extension of the Kalman filter to nonlinear systems,” presented at AeroSense’97, 1997, 182–193, International Society for Optics and Photonics.
- [119] Julier, S. J., “The scaled unscented transformation,” presented at Proceedings of the 2002 American Control Conference (IEEE Cat. No. CH37301), 2002, 4555–4559, IEEE.
- [120] Wan, E. A., Van Der Merwe, R., “The unscented Kalman filter for nonlinear estimation,” *Adapt. Syst. Signal Process. Commun. Control Symp. 2000 -SPCC IEEE 2000*, 153–158, Ieee (2000).
- [121] Hoag, D., “Apollo guidance and Navigation: Considerations of apollo imu gimbal lock,” *Cambridge MIT Instrum. Lab.*, 1–64 (1963).

- [122] “rlabbe/filterpy.”, GitHub, <<https://github.com/rlabbe/filterpy>> (18 July 2016).
- [123] “Phidgets Inc. - 1044_0 - PhidgetSpatial Precision 3/3/3 High Resolution.”, <http://www.phidgets.com/products.php?product_id=1044> (18 July 2016).
- [124] Lasso, A., Heffter, T., Rankin, A., Pinter, C., Ungi, T., Fichtinger, G., “PLUS: Open-Source Toolkit for Ultrasound-Guided Intervention Systems,” IEEE Trans. Biomed. Eng. **61**(10), 2527–2537 (2014).

UTSAV PARDASANI

OBJECTIVE

CONTRIBUTE SYSTEMS-LEVEL EXPERTISE IN THE DESIGN OF SOFTWARE AND HARDWARE TO SUPPORT EARLY STAGE PRODUCT DEVELOPMENT IN COMPUTER-ASSISTED MEDICAL INTERVENTIONS

TECHNICAL INTERESTS

- MEDICAL DEVICE R&D
- PRODUCT DEVELOPMENT
- MEDICAL ROBOTICS
- COMPUTER-ASSISTED ULTRASOUND IMAGING
- MR IMAGING
- MULTI-MODAL MEDICAL IMAGE VISUALIZATION SOFTWARE

EDUCATION

- | | |
|----------|--|
| CURRENT | <p>MASTERS OF ENGINEERING SCIENCE - BIOMEDICAL ENGINEERING <i>University of Western Ontario, LONDON, ON</i> <i>Thesis: A Multi-Sensor Image-Registration Fusion Approach to Tracking Ultrasound Probes</i></p> |
| APR 2009 | <p>BACHELORS OF APPLIED SCIENCE - MECHATRONICS ENGINEERING <i>University of Waterloo, WATERLOO, ON</i> <i>Capstone project: Robotic Laparoscopy</i></p> |

EXPERIENCE

SCIENTIFIC DEVELOPER - MITACS ACCELERATE INTERNSHIP

- | | |
|----------|--|
| JAN 2016 | ALGORITHM TEAM |
| CURRENT | <p><i>Synaptive Medical - Toronto, ON</i></p> <p>Developing software feasibility prototypes for innovative new products to support computer-assisted medical interventions</p> <p>Conducting accuracy assessment protocols for image-guided surgery hardware</p> <p>Supporting demonstrations of prototype hardware</p> <p>Filed a patent for a novel ultrasound tracking system</p> |

GRADUATE RESEARCH ASSISTANT

- | | |
|----------|--|
| SEP 2014 | VIRTUAL AUGMENTATION AND SIMULATION FOR SURGERY AND THERAPY LAB |
| CURRENT | <p><i>University of Western Ontario Robarts Research Institute - London, ON</i></p> <p>Developed a GPU-enabled Unscented Kalman Filter algorithm, fusing ultrasound-MRI registration, optical tracking, and inertial measurements for tracking ultrasound probes in image-guided neurosurgery</p> <p>Developed a websocket-enabled virtual reality plug-in for 3D Slicer supporting Google Cardboard and the Oculus Rift</p> |

MECHANICAL DEVELOPERMAY 2009 | **ADVANCED PRODUCT DEVELOPMENT**SEP 2014 | *Hologic - Sentinelle Division | Formerly Sentinelle Medical Inc - Toronto, ON*

Led mechanical and systems engineering activities for the Aegis Navigation MRI-ultrasound fusion system throughout the entire product lifecycle per ISO 13485 from conception to end-of-life

Developed a variety of multi-modal medical imaging phantoms

Developed mechanical components in Solidworks with close involvement from Industrial Design (drafting, GD&T, tolerance stack-up, etc.)

Created software prototypes for a new innovative product (ClearCanvas, GLSL, C#)

Developed feasibility prototype systems and development plans for potential image-guided products

Fabricated prototype hardware using a variety of methods (CnC milling, 3D printing, casting, thermoforming, etc.)

Supported clinical trials with prototype equipment, documentation, verification activities, applications training and technical support

Co-ordinated external safety testing and verification. (IEC 60601)

Developed and maintained product technical file for CE marking

Maintained product Device Master Record and Design History File

Visited hospitals to evaluate system performance and clinical workflows

Supported bulk bill of material updates for material compliance efforts

Prepared demonstration hardware for the Radiological Society of North America conference, as well as other tradeshows

Supported software testing and requirements definition

Developed training plans and work instructions for service and production

ROBOTIC SYSTEMS DESIGNERMAY 2008 | **ENGINEERING**AUG 2008 | *2G Robotics Inc - Waterloo, ON*

Designed and optimized electrical and mechanical components for an Autonomous Underwater Vehicle (AUV) to meet size constraints

Designed electrical components in EAGLE CAD

Troubleshooted microcontroller boards

Developed 3D visualization software to support underwater laser scanning product

R&T CONTROLS AND INSTRUMENTATION STUDENTSEP 2007 | **ADVANCED TECHNOLOGY**DEC 2007 | *Messier-Dowty Inc. Ajax, ON*

Technical lead on the research and development of an innovative smart sensor

Supported research in the development of a safety-critical redundant avionics bus

MISSION SYSTEMS ENGINEERING STUDENT

JAN 2007 | MISSION SYSTEMS ENGINEERING

APR 2007 | *MacDonald Dettweiler and Associates Space Missions - Brampton, ON*

Prepared and ran thermal simulations of the Space Station Remote Manipulator System (SSRMS, or Canadarm 2) to verify proposed manoeuvres on the International Space Station in orbit

Researched possible failure modes for SSRMS manoeuvres

Maintained and updated engineering requirements specifications

Prepared support drawings for customers

Analyzed engineering drawings and documentation to verify fastener specifications

Prepared documentation for the assembly of the Special Purpose Dexterous Manipulator

RESEARCH ASSOCIATE

MAY 2006 | HAND AND UPPER LIMB CENTRE

AUG 2006 | *Lawson Health Research Institute - London, ON*

Wrote visualization software incorporating magnetic and optical 6-degree of freedom tracking equipment in LabVIEW that enabled surgical guidance of orthopaedic procedures on cadaveric specimens

RESEARCH ASSOCIATE

SEP 2005 | HAND AND UPPER LIMB CENTRE

DEC 2005 | *Lawson Health Research Institute - London, ON*

Developed specifications for load cells for use in the biomechanics testing simulator

Troubleshooted control software and hardware for driving pneumatic actuators in the biomechanics testing simulator

Developed drivers and control software for SmartMotor SM servo motors

Evaluated applicability of servo-motors in custom lab-equipment

Integrated 3D visualization capabilities using VTK into LabVIEW via libraries written in C

Characterized servo motor performance and applicability for use in biomechanics testing simulator

RESEARCH ASSISTANT

SEP 2005 | CANADIAN SURGICAL TECHNOLOGIES AND ADVANCED ROBOTICS

DEC 2005 | AND VASST LAB, *Robarts Research Institute - LONDON, ON*

Researched the use of high performance graphics hardware for image processing computations

Developed visualization methods for aiding port selection in laparoscopic surgery in VTK and OpenGL

RESEARCH ASSISTANT

JUL 2004 | VIRTUAL AUGMENTATION AND SIMULATION FOR SURGERY AND THERAPY LAB

AUG 2004 | *Robarts Research Institute - London, ON*

Developed and evaluated image segmentation algorithms to identify hearts from MRI images

RESEARCH ASSISTANT

OCT 2002 | HAND AND UPPER LIMB CENTRE
 JAN 2003 | *Lawson Health Research Institute - London, ON*
 Developed kinematics visualization software in Python and VTK

GUEST WORKER

JUL 2001 | INTEGRATED MANUFACTURING TECHNOLOGIES INSTITUTE
 AUG 2001 | *National Research Council of Canada - London, ON*
 Implemented a two-way radio control system between a motor and a remote control
 Implemented a networked force feedback application with servo-motor

PUBLICATIONS

Jonathan Marmurek, Chris Wedlake, Utsav Pardasani, Roy Eagleson, Terry Peters.
Image Guided Laser Projection for Port Placement in Minimally Invasive Surgery. January 2006. Presented at Medicine Meets Virtual Reality 14 Conference.

Utsav Pardasani, John S.H. Baxter, Terry M. Peters, Ali R. Khan.
Single slice US-MRI registration for neurosurgical MRI-guided US. March 2016. Presented at the SPIE Medical Imaging 2015.

SCHOLARSHIPS

JAN 2016 - PRESENT | Mitacs Accelerate
 MAY 2014 - MAR 2016 | Ontario Graduate Scholarship (OGS)
 SEP 2014 - PRESENT | University of Western Ontario Graduate Research Scholarship (WGRS)
 SEP 2014 - APR 2014 | Computer-Assisted Medical Interventions Program (funded by NSERC's Collaborative Research and Training Experience Program)
 SEP 2004 | University of Waterloo Entrance Scholarship

SELECTED TECHNICAL SKILLS

- MEDICAL DEVICE PRODUCT LIFECYCLE MANAGEMENT AND RELATED PROCESSES
- PROGRAMMING (C++, C, C#, PYTHON, OPENGL, CUDA)
- MECHANICAL DESIGN
- DRAFTING & TOLERANCING
- SOLID MODELLING (SOLIDWORKS, CATIA, AUTOCAD)
- SIMULATION (MATLAB, SIMULINK, LABVIEW)
- MEDICAL IMAGE VISUALIZATION (VTK, SLICER, CLEARCANVAS)
- CNC & 3D PRINTER OPERATION
- PROJECT ENGINEERING
- LINUX AND UNIX-LIKE SYSTEMS
- EMBEDDED SOFTWARE

SELECTED UNIVERSITY COURSES

* = MASTER'S LEVEL

- IMAGE PROCESSING*
- MEDICAL IMAGING*
- RESEARCH ETHICS AND BIOSTATISTICS*
- BIOMECHANICS
- SYSTEMS MODELLING
- MACHINE DESIGN
- REAL TIME OPERATING SYSTEMS
- SENSORS AND INSTRUMENTATION
- DIGITAL CONTROL SYSTEMS